Formation of Amphibole-Bearing Peridotite and Amphibole-Bearing Pyroxenite through Hydrous Melt-Peridotite Reaction and In Situ Crystallization: An Experimental Study

Chunguang Wang[1, 2, *], Yan Liang[2], and Wenliang Xu[1]

[1] College of Earth Sciences, Jilin University, Changchun 130061, China

[2] Department of Earth, Environmental and Planetary Sciences, Brown University, Providence, RI 02912, USA

Corresponding author: Chunguang Wang (c_wang@jlu.edu.cn)

Key Points:

- Consequence of hydrous melt-peridotite reaction followed by in-situ crystallization was investigated experimentally.

- Hydrous melt-lherzolite reactive crystallization forms amphibole-bearing peridotite and amphibole-bearing pyroxenite.

- Chemical composition of amphibole can be used to identify hydrous melt and peridotite interaction in the upper mantle.

Abstract

16
17   Amphibole is a common hydrous mineral in mantle rocks. To better understand the
18   processes leading to the formation of amphibole-bearing peridotites and pyroxenites in mantle
19   rocks, we have undertaken an experimental study reacting lherzolite with hydrous basaltic melts
20   in Au-Pd capsules using the reaction couple method. Two melts were examined, a basaltic
21   andesite and a basalt, each containing 4 wt% of water. The experiments were run at 1200°C and
22   1 GPa for 3 or 12 h, and then cooled to 880°C and 0.8 GPa over 49 h. The reaction at 1200°C
23   and 1 GPa produced a melt-bearing orthopyroxenite-dunite sequence. The cooling stimulates
24   crystallization of orthopyroxene, clinopyroxene, amphibole, and plagioclase, leading to the
25   formation of an amphibole-bearing gabbronorite–orthopyroxenite–peridotite sequence.
26   Compositional variations of minerals in the experiments are controlled by temperature, pressure,
27   and reacting melt composition. Texture, mineralogy, and mineral compositional variation trends
28   obtained from the experiments are similar to those from mantle xenoliths and peridotite massif
29   from the field including amphibole-bearing peridotites and amphibole-bearing pyroxenite and
30   amphibolite that are spatially associated with peridotites, underscoring the importance of hydrous
31   melt-peridotite reaction in the formation of these amphibole-bearing rocks in the upper mantle.
32   Amphiboles in some field samples have distinct textual and mineralogical features and their
33   compositional variation trends are different from that defined by the melt-peridotite reaction
34   experiments. These amphiboles are either crystallized from the host magma that entrained the
35   xenoliths or product of hydrothermal alterations at shallow depths.

1. Introduction

37   Amphibole is commonly observed in mantle xenoliths (e.g., Wilshier and Schwarzman,
38   1971; Dautria et al., 1987; Moine et al., 2001; Xu et al., 2010) and massif peridotites (e.g.,
39   Agrinier et al., 1993; Zanetti et al., 1996; Ohara and Ishii, 1998; Li et al., 2018) from a range of
40   geological settings, such as arcs (e.g., Ohara and Ishii, 1998; Ishimaru et al., 2007; Bénard and
41   Ionov, 2013), ocean islands (e.g., Clague and Bohrson, 1991; Moine et al., 2001), continental
42   margins (Francis, 1976a, 1976b; Agrinier et al., 1993), and intracontinental regions (e.g.,
43   Wilshier and Schwarzman, 1971; Dautria et al., 1987; O'Reilly et al., 1991; Xu et al., 2010).
44   Typical lithologies include amphibole-bearing peridotite, amphibole-bearing pyroxenite, and
45   amphibolite. In general, amphibole occurs either interstitial to anhydrous minerals in peridotites
46   or in amphibole-rich veins or bodies in peridotites.

47   Based on field studies, a number of mechanisms have been proposed for the formation of
48   amphibole in mantle xenoliths and massif peridotites. Frey and Prinz (1978) reported a set of
49   amphibole-bearing peridotite and pyroxenite xenoliths in basanites from Grand Canyon and San
50   Carlos, Arizona, USA. They suggested that the poikilitic amphiboles enclosing olivines and
51   spinels were accumulations of basaltic magma. Agrinier et al. (1993) described different types of
52   amphibole in a peridotite massif from Zabargad Island, Red Sea. Amphiboles that exist as
53   individual grains interstitial between olivines and spinels were inferred to be products of reaction
54   between the peridotites and hydrous fluids, and amphiboles that occur in shear zones and
55   mylonitic bands to be results of seawater alteration after emplacement of the massif. Coltorti et
56   al. (2004) and Bonadiman et al. (2014) inferred that the disseminated amphiboles and vein
57   amphiboles in peridotite entrained by basalts from Victoria Land, Antarctica were formed by
58   reaction between clinopyroxene and a batch of metasomatic melt. The different occurrences are
59   due to different melt-to-rock ratios. The chief objective of the present study is to develop a set of

60   criteria that can be used to distinguish amphiboles formed by hydrous melt and peridotite
61   reaction from those produced by fluid-peridotite interaction or hydrothermal alteration.

62   The processes and consequences of melt-peridotite interaction have been extensively
63   studied through laboratory dissolution experiments for a range of starting compositions and P-T
64   conditions in anhydrous systems (e.g., Daines and Kohlstedt, 1994; Yaxley and Green, 1998;
65   Takahashi and Nakajima, 2002; Morgan and Liang, 2003, 2005; Beck et al., 2006; Lambart et
66   al., 2009, 2012; Van den Bleeken et al., 2010, 2011; Wang et al., 2013). However, comparable
67   studies in hydrous systems are limited (Sekine and Wyllie, 1983; Carroll and Wyllie, 1989;
68   Johnston and Wyllie, 1990; Kelemen et al., 1990; Sen and Dunn, 1994; Rapp et al., 1999; Mallik
69   et al., 2015; Mandler and Grove, 2016; Wang et al., 2016). Sen and Dunn (1994) conducted
70   reaction experiments by packing a powdered spinel lherzolite layer against a powdered
71   amphibolite (1.5 wt% water) layer in graphite-lined Pt capsules at 1.5-2.0 GPa and 950-1025°C.
72   They observed amphiboles along the boundaries of olivine, pyroxenes, and spinel. The
73   amphiboles have compositions similar to those in amphibole-bearing peridotite from the field.
74   They inferred that reaction of olivine, primary orthopyroxene, clinopyroxene, and spinel with
75   hydrous melt forms amphibole and Fe-rich orthopyroxene and that a further reaction would form
76   amphibole-bearing harzburgite (free of clinopyroxene and spinel) and finally amphibole-bearing
77   orthopyroxenite (free of clinopyroxene, spinel, and olivine). In a recent melt-peridotite reaction
78   study (Wang et al., 2016), we reacted a layer of lherzolite with a layer of water-added (4 wt%)
79   basaltic andesite in a Au-Pd lined graphite capsule at 1200°C and 1 GPa (run BAH8 in Wang et
80   al., 2016). Figure 1a is a back-scattered electron (BSE) image showing the orthopyroxenite-
81   dunite sequence formed in the peridotite half of the reaction couple and quenched amphibole
82   crystals in the interstitial melts around the orthopyroxenite-dunite boundary. The presence of
83   quenched amphiboles in this isothermal hydrous melt-peridotite reaction experiment is
84   intriguing. The reacting melt around the orthopyroxenite must be near amphibole saturation at
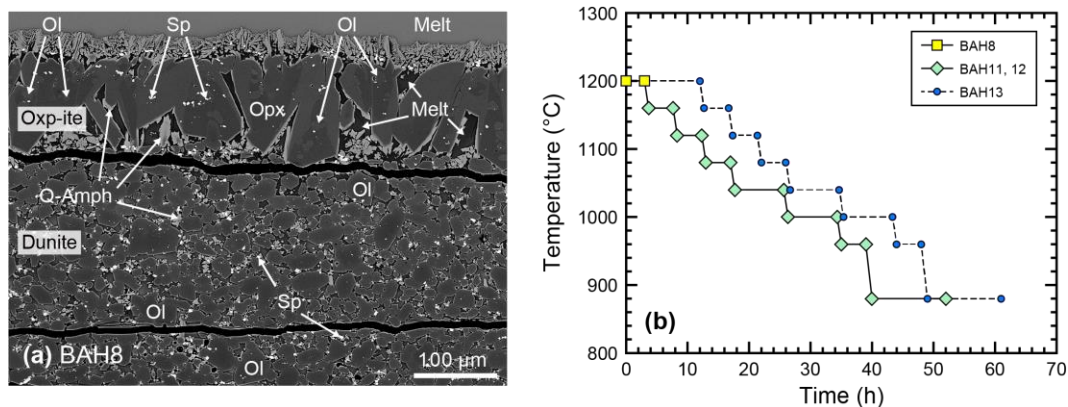85   1200°C and 1 GPa.

86

87 **Figure 1.** (a) Back-scattered electron (BSE) image that recalls the result (interface region) of hydrous basaltic
88 andesite and peridotite reaction experiments conducted at 1200 °C and 1 GPa (BAH8, Wang et al., 2016) using the
89 same capsule setup as those in the present study. Ol = olivine; Opx = orthopyroxene; Sp = spinel; Q-Amph = quench
90 amphibole; Opx-ite = orthopyroxenite. (b) Temperature histories of the melt-rock reaction experiments. Zero time
91 marks the beginning of the experiment, when the target temperature of 1200°C was reached. Experiments BAH11
92 and MBH12 were run using the same temperature-pressure path. BAH13 was hold at 1200°C for a longer duration
93 (12 h) than BAH11 and MBH12 (3 h). Temperature and duration used in the isothermal experiment BAH8 (1200°C,
94 3 h, without step cooling, Wang et al., 2016) is also shown for comparison.

95   In this study, we further expand the isothermal hydrous melt-peridotite reaction
96 experiments of Wang et al. (2016) by considering two hydrous melts (basalt and basaltic
97 andesite) and by allowing in situ crystallization of reacting melts through step cooling of
98 experimental charges (to 880°C and 0.8 GPa) at the end of isothermal reaction at 1200°C and 1
99 GPa (Fig. 1b). The quenched experimental charge enables us to examine the texture, mineralogy,
100 and mineral compositional variation formed after the hydrous melt and peridotite reaction.
101 Results from these experiments allow us to better understand the processes leading to the
102 formation of amphibole-bearing peridotites and pyroxenites.

103   The remaining part of this paper is organized as follows. In the next section, we describe
104 the starting materials and experimental methods. We present the textural and chemical features
105 of the run products, compare the results with those observed in previous experimental studies,
106 and discuss the processes leading to the formation of amphibole-bearing peridotites and
107 pyroxenites. We then compare texture and mineral compositions observed in the experiments
108 with those from amphibole-bearing peridotites and pyroxenites in mantle xenoliths and massif
109 peridotites. We show that water and melt-peridotite reaction are important in determining the
110 lithology and mineral compositional variation in the mantle rocks.

Table 1 Starting compositions

Oxide (wt%)	Basaltic andesite MONT147	MORB D44A	Spinel lherzolite WFY-2[b]			
			Olivine	Opx	Cpx	Spinel
SiO_2	54.86	50.13	40.25	54.39	51.45	0.08
TiO_2	0.77	1.25	0.01	0.09	0.39	0.15
Al_2O_3	18.78	16.31	0.04	4.44	5.49	54.26
Cr_2O_3			0.03	0.39	0.81	12.83
FeO^a	8.96	8.85	9.82	6.25	2.93	10.87
MnO	0.21	0.17	0.12	0.12	0.11	0.15
MgO	3.66	8.72	48.41	32.46	16.27	20.50
CaO	8.80	12.50	0.09	0.88	20.55	0.01
Na_2O	3.08	2.63	0.00	0.12	0.98	0.02
K_2O	0.78	0.02	0.00	0.01	0.00	0.01
NiO			0.38	0.11	0.04	0.35
P_2O_5	0.14	0.08				
Total	100.04	100.66	99.15	99.26	99.02	99.23
Mg#	42.13	63.72	89.78	90.25	90.82	77.07
Cr#						13.69

Mg# = 100 × Mg/(Mg + Fe), atomic ratio; Cr# = 100 × Cr/(Cr + Al), atomic ratio; Opx = orthopyroxene; Cpx = clinopyroxene.
[a] Total Fe as FeO
[b] WFY-2 consists of 60 % olivine, 23 % opx, 12 % cpx, and 5 % spinel

2. Methods

112   Hydrous melt-peridotite reaction and in situ crystallization experiments were conducted
113 using the reaction couple method and a 19.1-mm piston-cylinder apparatus at Brown University.

114   Reaction couples were made by juxtaposing a powdered starting basalt layer against a powdered
115   spinel lherzolite layer at a length ratio of ~5:3 in Au-Pd lined graphite capsules. Each experiment
116   consists of four stages: pressurization to 1 GPa at room temperature, a dwell at 1200°C and 1
117   GPa, a subsequent step cooling to 880°C and 0.8 GPa, and a final dwell at 880°C and 0.8 GPa.
118   The starting melt and mineral compositions are listed in Table 1. Run conditions for each
119   experiment are listed in Table 2, and the temperature-time paths are shown in Fig. 1b.

2.1. Starting compositions

121   The starting lherzolite (sample WFY-2) was obtained by mixing optically clean olivine
122   (60%), orthopyroxene (23%), clinopyroxene (12%), and spinel (5%) from a disaggregated fertile
123   spinel lherzolite xenolith entrained by alkali basalt from Huinan, China. The starting materials
124   for the reacting melts are a basaltic andesite (sample Mont147) from Montserrat and a mid-ocean
125   ridge basalt (MORB, sample D44A) from Southern East Pacific Rise to which we added 4 wt%
126   water during sample loading. The starting lherzolite and basaltic andesite were used in
127   isothermal hydrous melt-rock reaction experiments of Wang et al. (2016), and the MORB was
128   used in anhydrous reaction and crystallization experiments of Tursack and Liang (2012) and
129   Saper and Liang (2014). Results from these earlier laboratory studies serve as references or
130   benchmarks for the hydrous reaction and crystallization experiments reported in this study. The
131   starting samples were ground separately in ethanol using an agate mortar and pestle for 2-4 h and
132   stored at 110°C before use.

2.2. Experimental procedures

134   The furnace assembly consists of a Au-Pd lined graphite capsule in a MgO sleeve
135   sandwiched between two crushable MgO spacers in Pyrex tubing, NaCl sleeve, and straight-
136   walled graphite heater. The cylindrical graphite capsule (6.5 mm OD, 7 mm long) was lined with
137   a Au_{75}-Pd_{25} inner capsule (3 mm OD, 2.8 mm ID, 5 mm long). To make a reaction couple, we
138   first packed the peridotite powder in the lower part of the Au-Pd capsule and filled the remaining
139   part of the capsule with the basaltic andesite or MORB powder. We then added deionized water
140   using a micro syringe and sealed the Au-Pd capsule using a micro arc welder immediately after
141   water loading. We weighed the capsule before and after each loading to ensure that the water-to-
142   basalt weight ratio is around 4:96 (i.e., 4 wt% water). The arc welder has a thin tungsten
143   electrode (0.6 mm in diameter) and operates under a stream of protective argon gas. It allows
144   pinpoint welding with a very small heat affected area. The weight loss due to the welding is less
145   than 0.5% (evaporation of water and Au-Pd alloy). Finally, we loaded the sealed Au-Pd capsule
146   in the graphite capsule and capped the graphite capsule with a 0.5 mm thick graphite lid. The
147   furnace assembly and capsule used in this study are the same as those used in experiments BAH8
148   and BADH15 in Wang et al. (2016). Oxygen fugacity of the experiments is maintained at -8 to -9
149   logarithmic unit, estimated using the method of Barr and Grove (2010).

150   To conduct a reaction experiment, the charge was cold pressurized to 1 GPa, followed by
151   heating to 1200°C at 75°C/min while maintaining pressure. The run was held at 1200°C and 1
152   GPa for 3 h for runs BAH11 and MBH12 and 12 h for BAH13. The run was then cooled to
153   880°C over 7 steps in 49 h (Fig. 1b). Each step cooling was performed at a rate of 1°C/min,
154   followed by a 4 or 8 h dwell at the specific temperature. The pressure, which was not adjusted
155   during cooling, gradually decreased to 0.8 GPa at the final dwell (880°C). At the end of
156   experiment, the charge was quenched by cutting the power supply while maintaining the

157   pressure. The heating and step cooling were operated through a Eurotherm controller, and
158   temperature was measured using a $W_{97}Re_3$-$W_{75}Re_{25}$ thermocouple with an uncertainty of 10°C
159   (Morgan and Liang, 2005). No friction correction was applied to the pressure. The retrieved
160   experimental charge was checked under a binocular microscope to ensure no crack in the Au-Pd
161   capsule. The capsule was then mounted in epoxy and polished gradually using a 600-mesh SiC
162   polishing paper in water until the cylindrical axis was exposed. During polish, the Au-Pd capsule
163   was checked using a microscope under reflecting light to ensure no leak exist; the exposed
164   surface was soaked in epoxy and stored in a vacuum chamber for several times, so that cracks
165   formed during quench were puttied. The exposed surface was finally polished to 1 µm finish for
166   electron microprobe analysis.

167   2.3. Microprobe analysis

168   Collection of back-scattered electron images and X-ray concentration maps and
169   measurements of mineral compositions were carried out using a Cameca SX-100 electron
170   microprobe at Brown University. An accelerating voltage of 20 kV and a beam current of 25 nA
171   were used to collect X-ray concentration maps. A 10 µm diameter beam was used for glass
172   analyses and a focused beam for mineral analyses. Accelerating voltage and beam current were
173   15 kV and 10 nA for glass analyses, 20 kV and 15 nA for plagioclase analyses, and 20 kV and 25
174   nA for olivine, pyroxene, amphibole, and spinel analyses, respectively. Sodium was analyzed
175   first with counting times of 10 s for peak and 5 s for background to minimize volatilization.
176   Counting times for other elements were 20-30 s for peak, and 10-15 s for background on each
177   side of the peak. Natural standards were used for calibration.

Table 2 Summary of experimental conditions

Run#	BAH8[a]	BAH11	BAH13	MBH12
Starting melt	Basaltic andesite	Basaltic andesite	Basaltic andesite	MORB
Pressure (GPa)	1	1 (0.8)[b]	1 (0.8)[a]	1 (0.8)[a]
Initial temp (°C)	1200 (3 h)[c]	1200 (3 h)[c]	1200 (12 h)[c]	1200 (3 h)[c]
Final temp (°C)		880 (12 h)[c]	880 (12 h)[c]	880 (12 h)[c]
Cooling process	Quench	Step cooling[d]	Step cooling[d]	Step cooling[d]
Total duration (h)	3	52	61	52
RBL lithologies	Glass	Amph gabbronorite	Amph gabbronorite	Amph gabbronorite
	Opx-ite	Amph-bearing opx-ite	Amph-bearing opx-ite	Amph-bearing opx-ite
	Dunite	Amph-bearing harz	Amph-bearing harz	Amph-bearing lherz

RBL = reactive boundary layer; Amph = amphibole; Opx-ite = orthopyroxenite; Harz = harzburgite; Lherz = lherzolite.
[a] Isobaric and isothermal experiment from Wang et al. (2016)
[b] Number in parenthesis is the pressure at final temperature
[c] Number in parenthesis is the duration at the initial or final temperature
[d] Step cooling is at a rate of 1°C/min to specific temperatures maintained for 4 or 8 h

178 **3. Results and discussion**

179   Three hydrous melt-peridotite reaction and crystallization experiments were conducted
180   using the two starting melts. They were built on melt-peridotite reaction experiments using
181   similar setups and starting compositions that are either hydrous but isothermal (Wang et al.,
182   2016) or step-cooling but anhydrous (Tursack and Liang, 2012; Saper and Liang, 2014).

183 Experiments BAH11 and BAH13 use the 4 wt% water-added basaltic andesite as the starting
184 melt, and experiment MBH12 uses the 4 wt% water-added MORB as the starting melt. We did
185 not measure water contents in the experimental glasses because of the crystalline nature of the
186 experimental charges. Judging from the presence of amphibole and vesicles in the experiments
187 and integrity of the Au-Pd capsules (Fig. 2 and supporting Figure S1), we conclude that these
188 capsules retained a significant fraction of water in the system and our reacting melts were indeed
189 hydrous at run conditions. Mineralogical and textural features of the experiments are
190 summarized in Table 2. Representative BSE images of the run products are displayed in Figs. 2
191 and 3. Mineral compositions that were obtained from spot microprobe analyses are presented in
192 Figs. 4-10, and 12. Additional BSE images and mineral composition profiles (Figures S1-S8) can
193 be found in the Supporting Information, and electron microprobe data are archived at Mendeley
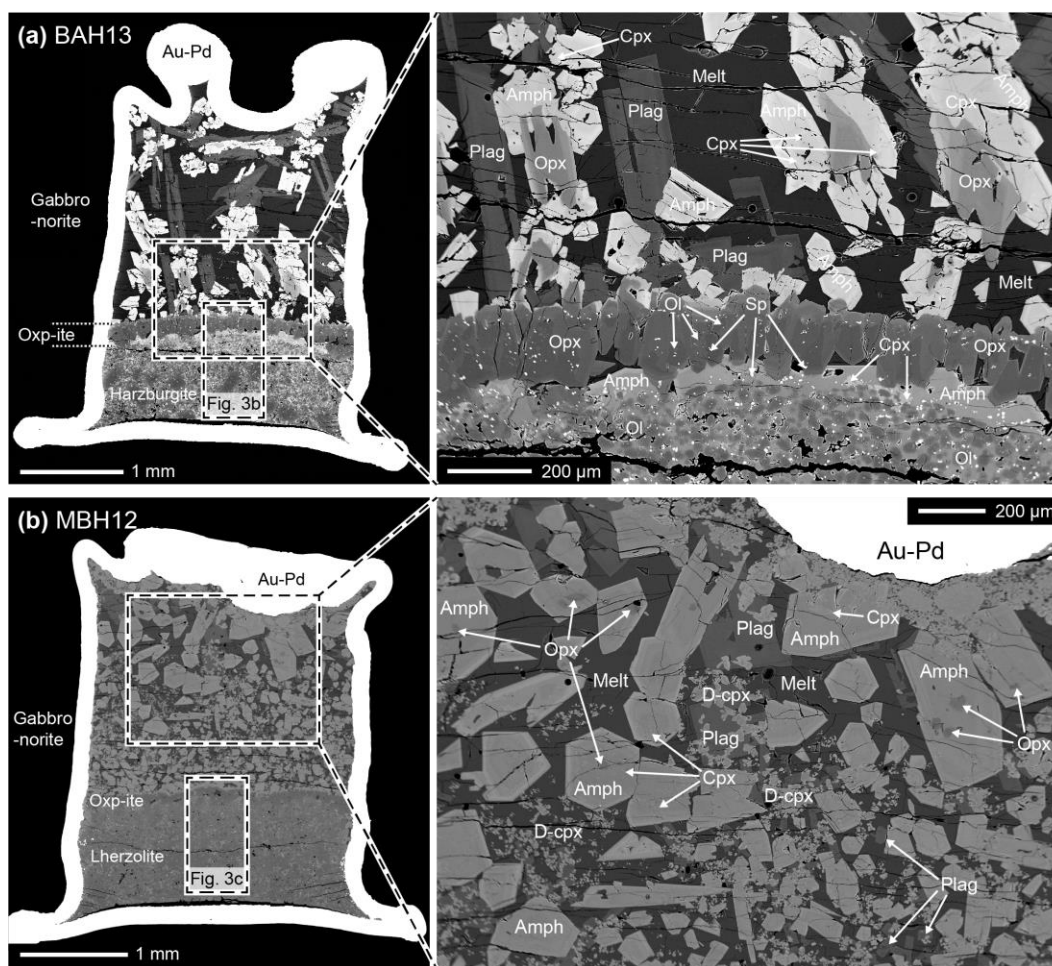194 Data (http://dx.doi.org/10.17632/895f6y8chd.1).

195
196 **Figure 2.** Back-scattered electron (BSE) images showing the results of the reactive crystallization experiments. (a)
197 BAH13 (hydrous basaltic andesite vs. lherzolite, 12 h reaction). (b) MBH12 (hydrous MORB vs. lherzolite, 3 h
198 reaction). The left panels are the entire experimental charges, and the right panels are the views of the gabbronorite
199 regions. Ol = olivine; Opx = orthopyroxene; Cpx = clinopyroxene; D-cpx = disseminated clinopyroxene; Sp =
200 spinel; Amph = amphibole; Plag = plagioclase; Opx-ite = orthopyroxenite.

201   3.1. Lithologies and textures

202   After reaction at 1200°C and 1 GPa and step cooling to 880°C and 0.8 GPa, each
203   experimental charge consists of three distinct lithological zones: an amphibole gabbronorite, an
204   amphibole-bearing peridotite, and an amphibole-bearing orthopyroxenite (100-300 μm thick)
205   that separates the former two lithological zones (Fig. 2 and Figure S1). The amphibole
206   gabbronorite, which is absent in the isothermal experiments of Tursack and Liang (2012) and
207   Wang et al. (2016), consists of orthopyroxene, clinopyroxene, amphibole, plagioclase, and
208   quenched melt (Fig. 2). Orthopyroxenes are subhedral and often surrounded by large euhedral
209   amphiboles or present as inclusions around the central part of amphiboles (Fig. 2 and Figure S1).
210   Clinopyroxene grains are anhedral and small. They are generally enclosed around rim parts of
211   the large amphiboles, and some clinopyroxenes in gabbronorite from MBH12 are dispersed in
212   melt or enclosed in plagioclases (Fig. 3b). Plagioclases are tabular-shaped with modal abundance
213   decrease from Runs BAH11 and BAH13 to Run MBH12. Ulvöspinel is observed in the
214   gabbronorite section in experiment BAH11 (Figure S1), a byproduct of reactive crystallization at
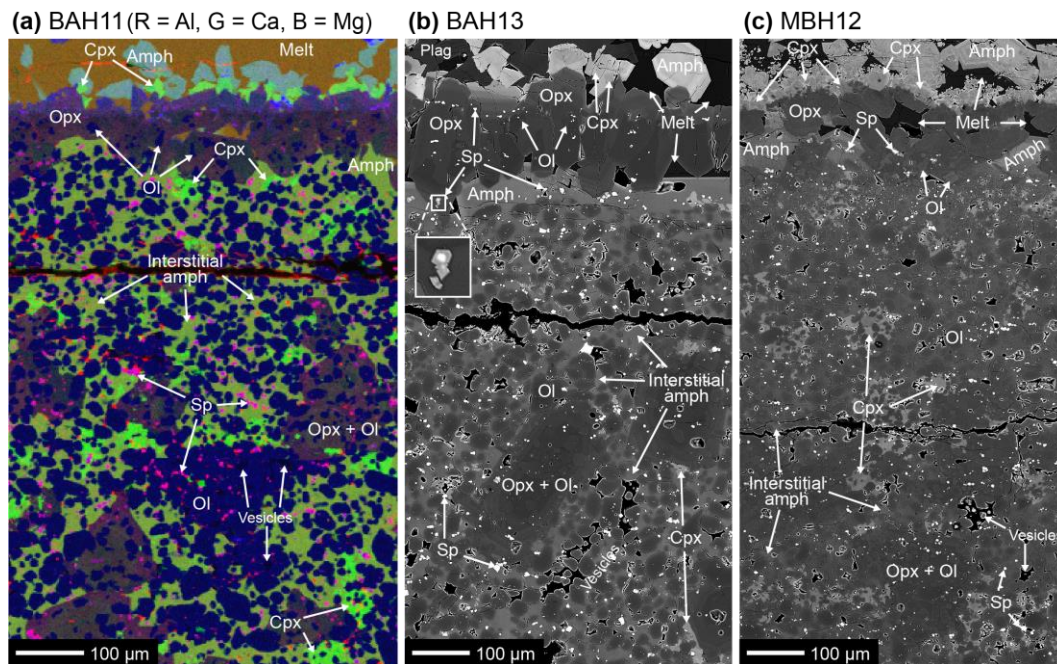215   the reducing condition.

216

217   **Figure 3.** False-colored composite X-ray concentration map (a) and back-scattered electron (BSE) images (b and c)
218   showing the amphibole-bearing orthopyroxenite and peridotite regions of experimental charges. (a) BAH11 (hydrous
219   basaltic andesite vs. lherzolite, 3 h reaction). (b) BAH13 (hydrous basaltic andesite vs. lherzolite, 12 h reaction). (c)
220   MBH12 (hydrous MORB vs. lherzolite, 3 h reaction). Ol = olivine; Opx = orthopyroxene; Cpx = clinopyroxene; Sp
221   = spinel, Amph = amphibole; Plag = plagioclase.

222   The amphibole-bearing peridotite consists of olivine, orthopyroxene, clinopyroxene,
223   spinel, and amphibole (Fig. 3). Olivines are round in shape and small in size (<60 μm in
224   diameter). Orthopyroxenes are large (up to 350 μm in length) and core-to-rim zoned in the X-ray
225   concentration map and BSE images (Fig. 3). The orthopyroxenes enclose small rounded olivines
226   and spinels forming a poikilitic texture. Clinopyroxenes are embayed in shape and low in modal
227   abundance (<7 vol%). Clinopyroxene is more abundant in the peridotite when the reacting melt
228   is the hydrous MORB (run MBH12) than those when the reacting melt is the hydrous basaltic

229 andesite (BAH11 and BAH13, cf. Fig. 3c to Figs. 3a and 3b). Some spinels exhibit euhedral
230 darker rims in the BSE images (insert in Fig. 3b). Amphibole is crystallized interstitial to other
231 minerals throughout the peridotite. Empty vesicles are present where small olivine grains are
232 abundant, but absent in the poikilitic orthopyroxenes. Plagioclase and interstitial melt are not
233 observed in the peridotite region.

234 The amphibole-bearing orthopyroxenite layer between the amphibole gabbronorite and
235 peridotite is mainly composed of large euhedral orthopyroxenes (up to 200 μm in length) (Fig.
236 3). These orthopyroxene grains contain small olivine and spinel inclusions (Fig. 3), similar to
237 those formed in the isothermal hydrous reaction experiment BAH8 from Wang et al. (2016).
238 Clinopyroxene and amphibole are observed around the gabbronorite-orthopyroxenite boundary,
239 whereas interstitial melt is observed around the orthopyroxenite-peridotite interface.
240 Interestingly, on the gabbronorite side of the orthopyroxenite in MBH12, orthopyroxenes are
241 partially dissolved and replaced by a layer of clinopyroxene (Fig. 3c), suggesting a reaction
242 relationship between the two minerals.

243 3.2. Variations in mineral composition

244 Compositional variations in minerals from the hydrous melt-peridotite reaction
245 experiments are observed both within grain and across lithological regions. Grain-scale variation
246 exists in orthopyroxene, amphibole, plagioclase, and spinel. Cores of large orthopyroxene and
247 amphibole grains have higher Mg# [Mg# = $100 \times$ Mg/(Mg + Fe), in molar] than the rims
248 (Figures S2 and S3). Plagioclase displays oscillatory zoning with an overall decreasing in An#
249 [An# = $100 \times$ Ca/(Ca + Na), in molar] and Al_2O_3 content from core to rim (Figure S4). Spinel
250 grains exhibit core-to-rim zoning in the BSE images (insert in Fig. 2b). The darker rims likely
251 have lower Cr# [Cr# = $100 \times$ Cr/(Cr + Al), in molar] and higher Mg# than the lighter cores.
252 These core-to-rim variations are consistent with crystallization trends.

253 Figures 4 and 5 display compositional variations of orthopyroxene and amphibole across
254 the gabbronorite, orthopyroxenite, and peridotite sequence. (Compositional profiles for other
255 minerals can be found in Figures S5-S8.) Zero distance marks the approximate position of the
256 gabbronorite-orthopyroxenite interface at the end of the run. This interface is also the boundary
257 separating the crystalline region (melt-bearing orthopyroxenite and dunite) and the crystal-free
258 reacting melt during the reaction at 1200°C (Fig. 1a). Mineral compositions are distinct across
259 the interface for both orthopyroxene and amphibole, although the trends are somewhat obscured
260 by core-to-rim variations. The differences are more pronounced in run BAH11 (basaltic andesite
261 as reacting melt, 3 h reaction at 1200°C, cyan symbols) than the other two runs (blue and red
262 symbols). For longer reaction time (BAH13) and more primitive reacting melt composition
263 (MBH12), compositions of amphiboles and orthopyroxenes in gabbronorite become more similar
264 to those in the peridotite. SiO_2 content in amphibole and Mg# in orthopyroxene and amphibole
265 from the gabbronorite layer are lower than those from the peridotite and orthopyroxenite layers,
266 whereas TiO_2 and MnO contents are higher in the gabbronorite. Na_2O abundance decreases in
267 orthopyroxenes (Fig. 4g) and increases in amphibole (Fig. 5h) from peridotite to gabbronorite.
268 Orthopyroxene and amphibole compositions from each experiment exhibit large variabilities at
269 the same distance in the compositional profiles, consistent with the core-to-rim compositional
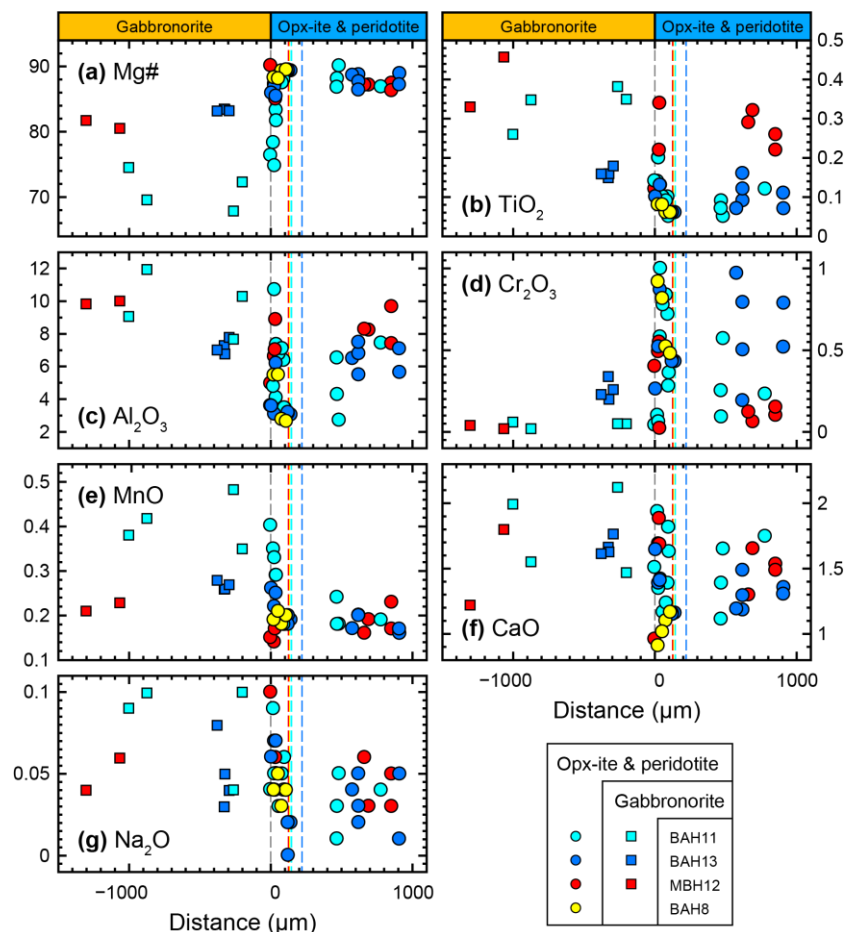270 variations (Figs. 4 and 5).

Figure 4. Plots of Mg# and oxide abundances (in wt%) in orthopyroxene as a function of distance from the gabbronorite-orthopyroxenite interface. Circles represent orthopyroxene in the amphibole-bearing orthopyroxenite (opx-ite) and peridotite regions, and squares represent those in the amphibole gabbronorite region of each experiment. Also shown are compositions of orthopyroxene in orthopyroxenite from the isothermal reaction experiment BAH8 from Wang et al. (2016). The dashed gray lines mark the position of gabbronorite-orthopyroxenite interface, and the dashed cyan, blue, red, and yellow lines mark the positions of orthopyroxenite-peridotite interfaces in BAH11, BAH13, BAH12, and BAH8, respectively.
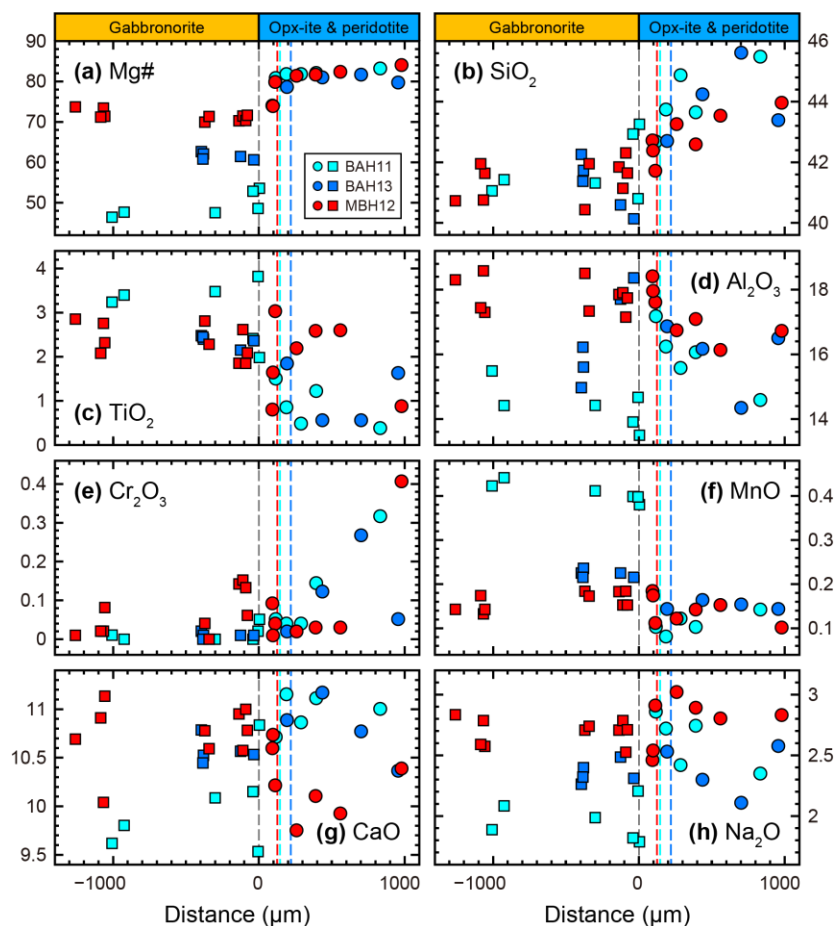
Figure 5. Plots of Mg# and oxide abundances (in wt%) in amphibole as a function of distance from the gabbronorite-orthopyroxenite interface. Circles represent amphibole in the amphibole-bearing orthopyroxenite (opx-ite) and peridotite regions, and squares represent those in the amphibole gabbronorite region of each experiment. The dashed gray lines mark the position of gabbronorite-orthopyroxenite interface, and the dashed cyan, blue, and red lines mark the positions of orthopyroxenite-peridotite interfaces in BAH11, BAH13, and BAH12, respectively.

3.3. Comparison with previous melt-rock reaction experiments

The lithological sequence and mineral compositions of the hydrous melt-peridotite reaction experiments are significantly different from those of the anhydrous cases that have nearly identical starting melt and peridotite compositions. The most remarkable difference between the hydrous reactive crystallization experiments presented here and the anhydrous ones reported by Tursack and Liang (2012) and Saper and Liang (2014) is the formation of amphibole-bearing orthopyroxenite and amphibole-bearing peridotite in the hydrous experiments (Figs. 2 and 3). The two anhydrous reactive crystallization studies (reaction at 1 GPa and 1300-1320°C, followed by a step cooling to 1200°C or 1050°C) used the same starting basalt (sample D44A) as the hydrous run MBH12 but without addition of water. These experiments produced a gabbronorite–wehrlite or a gabbronorite–wehrlite–peridotite sequence. Plagioclase is observed in the wehrlite and peridotite in experiments where the starting lherzolite was mixed with 12% basalt (Saper and Liang, 2014). Plagioclase is not observed in the peridotite layer in the present study.
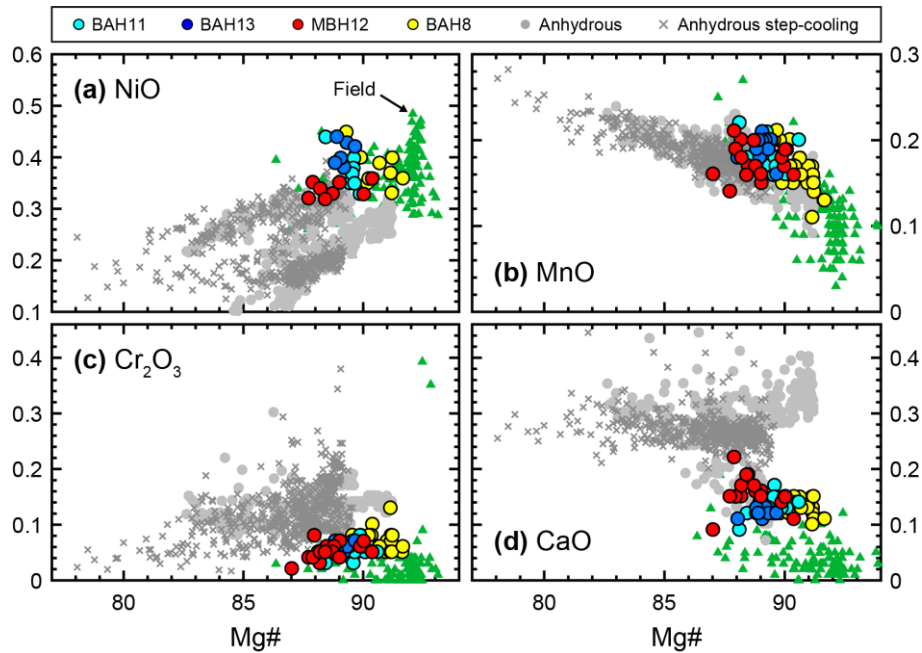
299

Figure 6. Variations of oxide abundances (in wt%) vs. Mg# in olivine from melt-peridotite reaction experiments and those from field observations of amphibole-bearing mantle rocks (green triangles). Color circles are olivines from the hydrous melt-peridotite reaction experiments BAH11, BAH13, and BAH12 from this study and BAH8 from Wang et al. (2016). Gray circles are olivines from anhydrous isothermal melt-peridotite reaction experiments (Harzdis24 from Morgan and Liang, 2003; Lherzdis4 and Lherzdis5 from Morgan and Liang, 2005; PDET1 from Tursack and Liang, 2012), and gray crosses are those from anhydrous reactive crystallization experiments (PDET1b, PDET1c, and PDET2b from Turack and Liang, 2012; PDLS6 and PDSL11 from Saper and Liang, 2014), all conducted in the same laboratory using similar experimental design and starting compositions. The Mantle xenoliths are from the North China Craton (Xu and Bodinier, 2004; Xu et al., 2010), western US (Wilshier and Schwarzman, 1971; Francis, 1976a, 1976b; Wilshier et al., 1980), Hawaii (Clagu and Bohrson, 1991), Antarctica (Coltorti et al., 2004; Bonadiman et al., 2014), southeastern Australia (O'Reilly et al., 1991; Powell et al., 2004), Kerguelen Islands (Moine et al., 2001), Rhenish Uplands (Witt and Seck, 1989; Witt-Eickschen et al. 2003), Avacha (Bénard and Ionov, 2013), and Ahaggar (Dautria et al., 1987). The massif peridotites are from Lherz (Zanetti et al., 1996), Mariana Trench (Ohara and Ishii, 1998), Zabargad Island (Agrinier, 1993), and Sulu Orogen (Li et al., 2018).

Figures 6-10 compare mineral compositions obtained from the hydrous melt-peridotite reaction experiments with those from the anhydrous ones (for olivine, pyroxenes, spinel, and plagioclase) and phase equilibrium experiments (for amphibole and plagioclase). In general, NiO is positively and MnO is negatively correlated with Mg# in olivine from the melt-rock reaction experiments (Figs. 6a and 6b). Olivine composition from the hydrous melt-rock reaction experiments covers a considerably narrower range than both the isothermal and the step-cooling experiments conducted under anhydrous conditions (Fig. 6). They cluster at the high-Mg# and high-NiO end in the NiO vs. Mg# diagram (Fig. 6a). Olivines from the hydrous experiments have lower CaO and Cr_2O_3 contents and slightly higher MnO content than those from the anhydrous ones (Figs. 6b-6d). Among the hydrous reaction experiments, olivine from the step-cooling ones (cyan, blue, and red circles in Fig. 6) have slightly lower Mg# than the hydrous isothermal one BAH8 (yellow circles in Fig. 6).
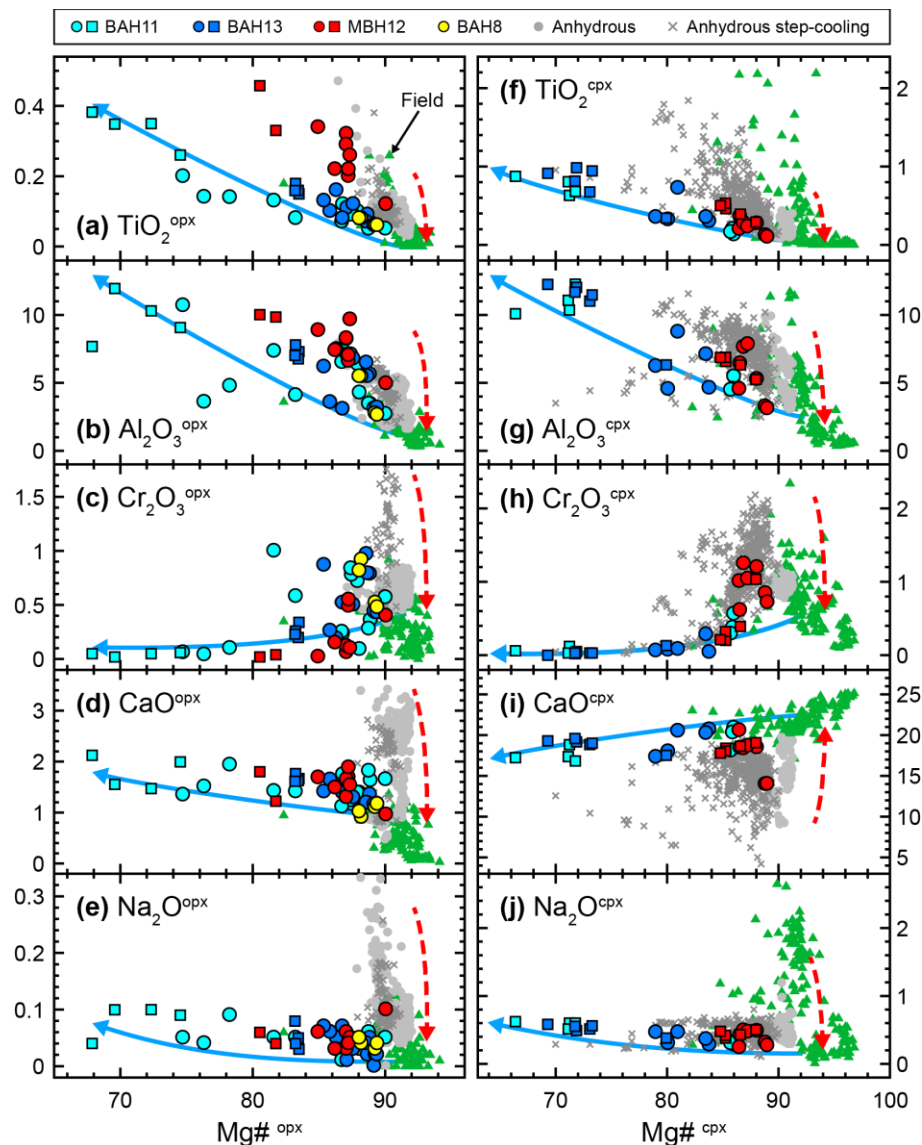
Figure 7. Variations of oxide abundances (in wt%) vs. Mg# in orthopyroxene (a-e) and clinopyroxene (f-j) from melt-peridotite reaction experiments and those from field observations of amphibole-bearing mantle rocks (green triangles). Circles are orthopyroxene in the amphibole-bearing orthopyroxenite and peridotite regions, and squares are those in the amphibole gabbronorite regions in experiments from this study. Source of the experimental and field data are the same as in Fig. 6. The dashed red arrows mark the melting and re-equilibration trend, and the solid blue arrows mark the melt-rock reaction-crystallization trend in orthopyroxene and clinopyroxene compositional variations.

Two types of variation trends are observed in orthopyroxene and clinopyroxene compositions from the melt-rock reaction experiments: the melting and reequilibration trend and the reaction-crystallization trend (Wang et al., 2013). The former is characterized by decreases of incompatible elements (e.g., TiO_2, Al_2O_3, and Na_2O) and a slight increase of Mg# in pyroxenes (dashed red arrows in Fig. 7), and the latter by gradual enrichments of the incompatible elements with a significant decrease of Mg# (blue arrows in Fig. 7). Compositions of orthopyroxene from the isothermal hydrous melt-rock reaction experiment BAH8 plot at the high-Mg# ends on the oxide-Mg# variation diagrams. Compositions of pyroxenes from the hydrous reactive crystallization experiments further expand the melt-rock reaction trend that are mainly

343 established by pyroxenes from the anhydrous reactive crystallization experiments of Tursack and
344 Liang (2012) and Saper and Liang (2014) with Mg# down to lower than 70.

345   Figure 8 plots Cr# against Mg# and TiO_2 content in spinel from the melt-rock reaction
346 experiments. Spinel from the hydrous reactive crystallization experiments is scattered in Cr# (6-
347 55), consistent with the observed core-to-rim variations in spinels from the hydrous reactive
348 crystallization experiments (inset in Fig. 3b). Spinels from the isothermal run BAH8 are plotted
349 at the high-Cr# end of data from the hydrous experiments. Mg# (46-61) and TiO_2 content (0.19-
350 0.40 wt%) in spinel from the hydrous experiments are relatively uniform, both lower than those
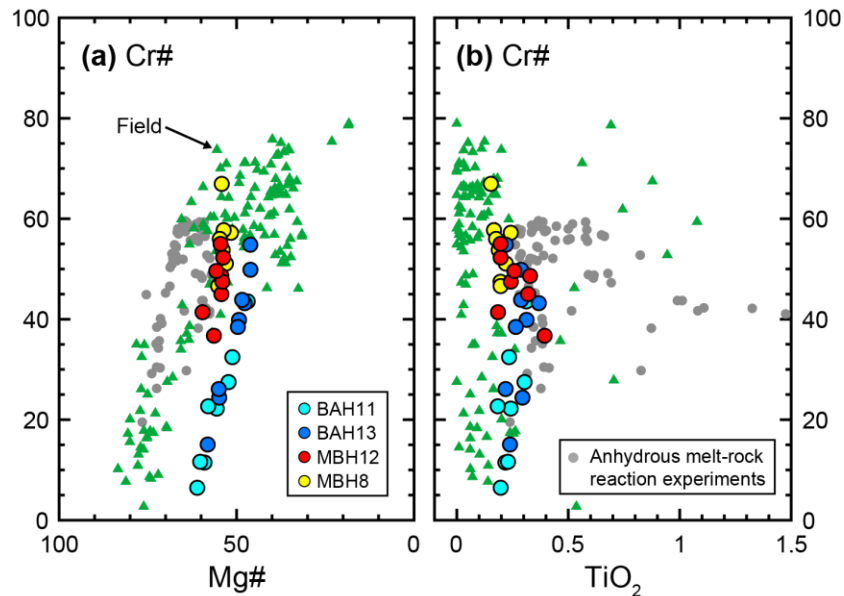351 in the anhydrous experiments.

352

Figure 8. Variations of Cr# as a function of Mg# or TiO_2 abundance (in wt%) in spinel from melt-peridotite reaction
experiments and those from field observations of amphibole-bearing mantle rocks (green triangles). Color circles are
spinels in experiments from this study. Gray circles are spinels from anhydrous reaction experiments (PDET1,
PDET1b, and PDET1c) of Turack and Liang (2012). Source of the field data are the same as in Fig. 6.

357   Figure 9 compares compositions of amphibole from this study with those from the melt-
358 peridotite reaction experiments of Sen and Dunn (1994), Mallik et al. (2015), and Mandler and
359 Grove (2016) that have low starting melt-to-peridotite ratios (gray triangles). Also shown in Fig.
360 9 are amphiboles from phase equilibrium experiments for hydrous basaltic and andesitic
361 compositions (plus symbols). Compositions of amphibole from the melt-rock reaction
362 experiments broadly vary along continuous trends (arrows), different from the phase equilibrium
363 experiments which have relatively scattered amphibole compositions. Amphiboles from the low
364 melt-to-peridotite ratio reaction experiments are plotted at the high-Mg# end (88-92) of the oxide
365 vs. Mg# variation diagrams. Amphiboles in the peridotite and orthopyroxenite regions from our
366 hydrous reaction experiments have lower Mg#, and those from the gabbronorite region have the
367 lowest Mg#. Amphiboles from phase equilibrium studies have lower Al_2O_3 and higher SiO_2 than
368 those from the melt-rock reaction experiments at a given Mg# (Figs. 9a and 9b), whereas they
369 broadly overlap the melt-rock reaction trends in the CaO, TiO_2, Na_2O, and MnO vs. Mg#
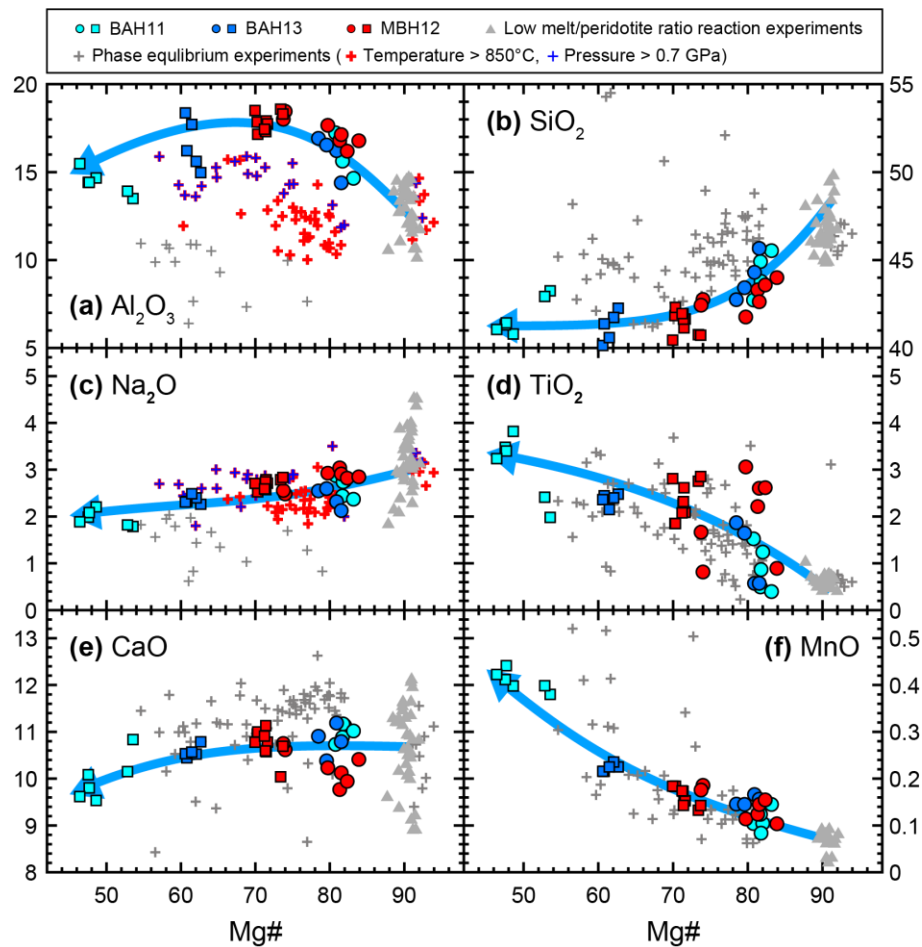370 diagrams (Figs. 9c-9f).

371

Figure 9. Variations of oxide abundances (in wt%) as a function of Mg# in amphibole from melt-peridotite reaction
experiments (circles, squares, and triangles) and phase equilibrium experiments (plus symbols, Nicholls and Harris,
1980; Green and Pearson, 1985; Latourrette et al., 1995; Feig et al., 2006; Mercer and Johnston, 2008; Parat et al.,
2008; Pietranik et al., 2009; Nandedkar et al., 2016). Circles are amphiboles in the amphibole-bearing
orthopyroxenite and peridotite regions, and squares are those in the amphibole gabbronorite region in reaction
experiments from this study (identical to those in Fig. 5). Triangles are amphiboles in the low melt-to-rock ratio
reaction experiments (Sen and Dun 1994; Mallik et al. 2015; Mandler and Grove 2016). Blue arrows mark the
amphibole compositional variation trends established by the melt-peridotite reaction experiments. Data from the
phase equilibrium studies are discriminated by experimental temperature and pressure in (a) and (c).

Figure 10 compares plagioclase compositions from melt-rock reaction experiments with
those from phase equilibrium experiments. Plagioclase compositions from the reaction
experiments are generally low in An#, FeO and MgO contents than the phase equilibrium
experiments except some experiments that were run at subsolidus conditions (Borghini et al.,
2010; Fumagalli et al., 2017). Plagioclase from hydrous melt-rock reaction experiments has
similar An# and Al_2O_3 and FeO contents to, but significantly lower MgO content than, those
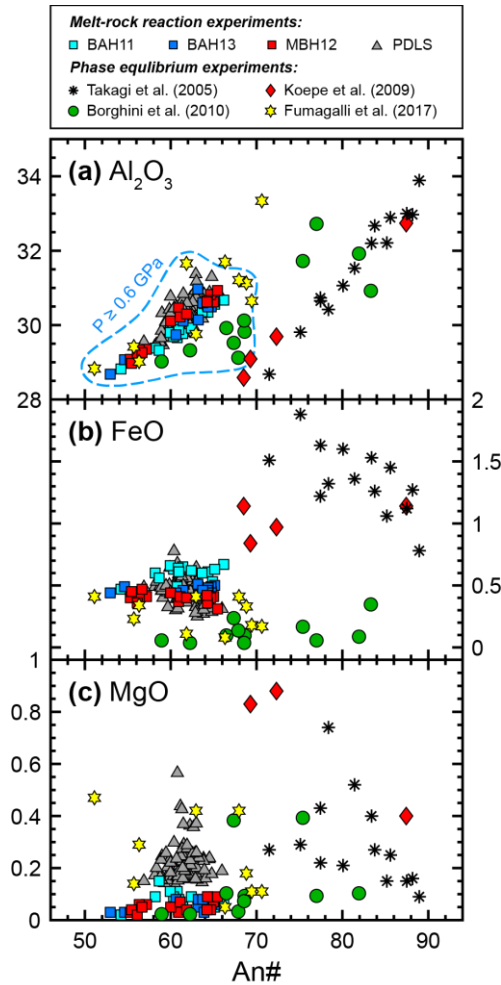from anhydrous ones in Saper and Liang (2014) (Fig. 10c).

Figure 10. Variations of Al_2O_3, FeO, and MgO abundances (in wt%) vs. An# in plagioclase from melt-peridotite reaction experiments and phase equilibrium experiments. The reaction experiments include those from this study and the anhydrous ones (PDLS) from Saper and Liang (2014). The phase equilibrium experiments are from Takagi et al. (2005), Koepke et al. (2009), Borghini et al. (2010), and Fumagalli et al. (2017). The dashed field in (a) shows the range of data from experiments that were run at pressures greater than 0.6 GPa.

3.4. Origin of texture and mineral compositional variations

Texture of the melt-rock reaction experiments depends on major element composition and water content of the reacting melt, and P-T-t history. Reaction between the hydrous basaltic andesite and lherzolite at 1200°C and 1 GPa produced a high-porosity orthopyroxenite-dunite sequence (run BAH8 in Wang et al., 2016). The dunite is formed by hydrous melting of lherzolite, and the orthopyroxenite is formed by reaction between olivine and the interface melt with orthopyroxene as the liquidus phase (Fig. 11a). Oversaturation of orthopyroxene in the hydrous reacting melt leads to the crystallization of orthopyroxene upon subsequent cooling, forming the orthopyroxene oikocrysts in the peridotite (Figs. 3 and 11b). Clinopyroxene and amphibole are near-liquidus phases of interstitial melts in the peridotite and orthopyroxenite. Stability of clinopyroxene on the liquidus increases from hydrous basaltic andesite to hydrous basalt (e.g., Weaver et al., 2011). This explains the more abundant clinopyroxene in run MBH12 than in runs BAH11 and BAH13, and the replacement of orthopyroxene by clinopyroxene around the gabbronorite-orthopyroxenite interface in MBH12 (Figs. 3 and 11c). Orthopyroxene

408 and clinopyroxene are surrounded by amphiboles (Figs. 2, 3, and 11d), suggesting the delayed
409 crystallization of the latter. In the anhydrous reactive crystallization experiments, clinopyroxene
410 is the main phase crystallized during cooling (Tursack and Liang, 2012) and plagioclase is
411 precipitated when melt infiltration is extensive (Saper and Liang, 2014). The presence of water in
412 reacting melt in the hydrous reactive crystallization experiments stabilizes amphibole which
413 crystallizes throughout the peridotite region (Fig. 3). Crystallization of amphibole is at the
414 expenses of clinopyroxene and hydrous melt, resulting in the embayed clinopyroxenes in the
415 peridotite and the small clinopyroxene inclusions near the rims of large amphiboles in the
416 gabbronorite (Figs. 3 and 11d). The empty vesicles formed during quench represent water
417 exsolved from interstitial melt upon cooling. Surface tension and capillary suction drive water to
418 the porous olivine matrix. The euhedral shape of plagioclase grains in the gabbronorite region
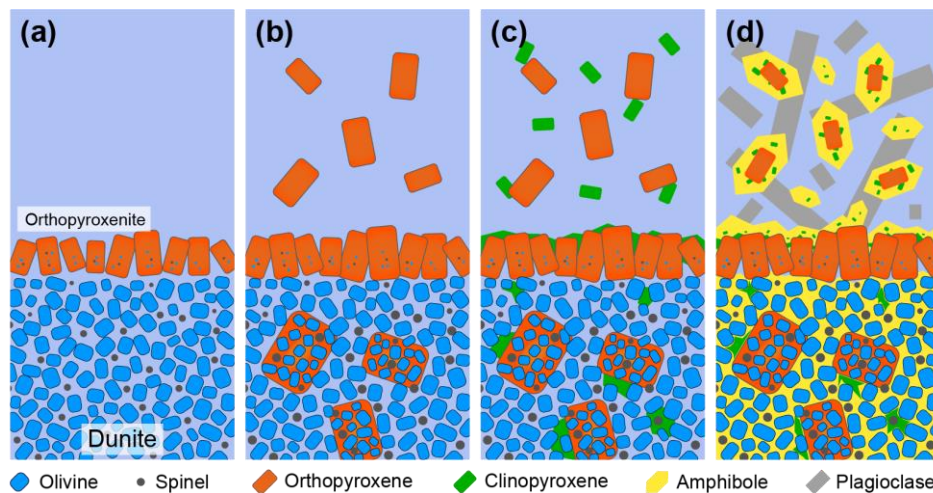419 suggests that plagioclase is the last phase of crystallization.

420

421 **Figure 11.** Schematic diagrams illustrating processes leading to the formation of amphibole-bearing gabbronorite –
422 orthopyroxenite – peridotite sequence in the hydrous melt and lherzolite reactive crystallization experiments. (a)
423 Formation of orthopyroxenite-dunite sequence by reaction between hydrous melt and peridotite at 1200°C (adapted
424 from Wang et al., 2016). (b-d) Successive crystallizations of orthopyroxene, clinopyroxene, amphibole, and
425 plagioclase during the step-cooling.

426 Mg# and NiO content in olivine are governed by extent of peridotite melting. The high
427 degree of peridotite melting promoted by hydrous melt infiltration at 1200°C accounts for the
428 higher Mg# and NiO contents in olivine from the hydrous experiments than those from the
429 anhydrous ones (Fig. 6a). The hydrous reaction experiments were run at relatively low
430 temperatures (1200°C with a cooling to 880°C) compared to the anhydrous ones (1300-1320°C
431 with a cooling to 1200°C or 1050°C or without), which gives rise to the lower CaO in olivine,
432 the lower CaO in orthopyroxene, and higher CaO in clinopyroxene from the hydrous
433 experiments than those in the anhydrous ones (e.g., Brey and Köhler, 1990; Köhler and Brey,
434 1990, Figs. 6 and 7). Such relationship between temperature and CaO in olivine and pyroxenes
435 has been also observed in previous melt-rock reaction studies (e.g., Wang et al., 2013, 2016;
436 Saper and Liang, 2014). Step-cooling expands the temperature ranges of the runs and hence the
437 larger ranges of Mg# in pyroxenes and Cr# in spinel along the melt-rock reaction trends in Figs.
438 7 and 8.

439 The variations in amphibole composition from the experimental studies can be attributed
440 to the differences in temperature, pressure, and melt composition. From the low melt-to-rock

441 ratio reaction experiments (Sen and Dunn, 1994; Mallik et al., 2015; Mandler and Grove, 2016)
442 to the peridotite and orthopyroxenite regions to the gabbronorite region in the present
443 experiments, Mg# in amphibole decreases, in accordant with the difference in melt composition
444 from which amphibole is crystallized (Fig. 9). The variation trends of TiO_2 and MnO versus Mg#
445 in amphibole from the melt-rock reaction experiments are broadly similar to those from the
446 phase equilibrium experiments (Figs. 9d and 9f), whereas Al_2O_3 and Na_2O in amphibole from the
447 reaction experiments are generally higher than those from the phase equilibrium experiments.
448 Al_2O_3 in amphibole increases with temperature (for tetrahedral Al) and pressure (for octahedral
449 Al) (e.g., Spear, 1981; Ernst and Liu, 1998; Larocque and Canil, 2010), and Na_2O in amphibole
450 increases with pressure (e.g., Ernst and Liu, 1998; Niida and Green, 1999). Amphibole from
451 experiments run at high temperatures (> 850°C) or at high pressures (> 0.7 GPa) has relatively
452 high Al_2O_3 content, and amphibole from experiments run at high pressures (> 0.7 GPa) has
453 relatively high Na_2O content (Fig. 9). These temperature- and pressure-dependent Al_2O_3 and
454 Na_2O variations are consistent with the grain-scale variations of amphibole composition: as
455 temperature and pressure decrease during step-cooling, the amphibole grows with decreasing
456 Al_2O_3 and Na_2O contents in the rim (Fig. S3). In spite of the numerous factors that control
457 amphibole composition during melt-rock reaction, the laboratory melt-rock reaction experiments
458 establish general variation trends (blue arrows in Figs. 9 and 12). As melt-rock reaction or
459 diffusive exchange between reacting melt and minerals becomes extensive, Mg# and Na_2O in
460 amphibole decrease, whereas MnO, TiO_2, and Al_2O_3 in amphibole increase.

461   Composition of plagioclase can be affected by temperature, pressure, and melt
462 composition (Longhi et al., 1976; Namur et al., 2012; Faak et al., 2013). As demonstrated by
463 Saper and Liang (2014), reaction of MORB with peridotite at a moderate pressure delays the
464 crystallization of plagioclase. Presence of water also delays plagioclase crystallization in basalts
465 (Takagi et al., 2005; Borghini et al., 2010; Namur et al., 2012). In our hydrous reactive
466 crystallization experiments, plagioclase is the last mineral to crystallize. This explains the
467 relatively low An# in plagioclase from these experiments, compared with that from the phase
468 equilibrium studies (Fig. 10a). Because of the late-stage crystallization (i.e., from an evolved
469 residual melt at low P and T), FeO and MgO contents in plagioclase from the reaction
470 experiments are low, comparable to those from the subsolidus phase equilibrium experiments of
471 Borghini et al. (2010) and Fumagalli et al. (2017) (Figs. 10b and 10c). In contrast, FeO and MgO
472 contents in plagioclase from the phase equilibrium experiments of Takagi et al. (2005) and
473 Koepke et al. (2005) are high (Figs. 10b and 10c), as it is the near-liquidus mineral in these
474 experiments.

4. Geological applications

476   The experiments reported here and those in Tursack and Liang (2012), Saper and Liang
477 (2014), and Wang et al. (2016) underscore the importance of water in the reacting melt in
478 determining the lithology and mineral compositional variations produced by melt-rock reaction
479 in the mantle. Hydrous basalts-peridotite reaction and in situ crystallization can produce a
480 spatially associated amphibole-bearing peridotite and amphibole-bearing orthopyroxenite
481 sequence. Because of the simplified experimental setup, the mass transfer mechanism may be
482 different between melt-peridotite interaction in the laboratory experiments and those in nature
483 (e.g., diffusion vs. advection). Extensive water infiltration into the powdered starting peridotite
484 lead to partial melting and faster reaction. The rate of cooling in the experiments is likely faster
485 than that takes place in nature. Nevertheless, the kinetics and compositional variation trends are

486   quite similar between the laboratory experiments and those in nature, because they are
487   determined by chemical potential gradients of the major components and phase relationships in
488   the hydrous basalt-peridotite system. The fast reaction and crystallization rates manifest grain-
489   scale processes and help to develop chemical variations on the laboratory time scale and length
490   scale. To assess the effect of hydrous melt-peridotite interaction in modifying composition and
491   mineralogy of the lithospheric mantle, we compare mineral compositions obtained from
492   laboratory melt-rock reaction experiments with those from the field in Figs. 6-9, and 12.
493   Calculation of chemical formula and nomenclature of the amphibole supergroup follow the
494   method described in Leake et al. (1997). We prefer to use this Si-Al-Na-K based amphibole
495   classification in this study because abundances and substitution of these elements are important
496   indications of melt composition and temperature and pressure conditions.

4.1. Olivine, pyroxenes and spinel in amphibole-bearing mantle rocks

498   Figures 6, 7 and 8 compare compositions of olivine, pyroxenes, and spinel obtained from
499   laboratory melt-peridotite reaction experiments with those in the amphibole-bearing mantle rocks
500   from the field. Compositional variations of these minerals from the field samples broadly follow
501   the trends established by the melt-peridotite reaction experiments, although clinopyroxenes from
502   the reaction experiments are lower in Mg# than the field data. The mismatch in Mg# between the
503   experimental data and the field data are also observed in the amphibole compositions (Figs. 12b
504   and 12e). These are in part due to the evolved nature of reacting melts and high melt-to-
505   peridotite ratios in the experiments and the subsolidus state of the natural samples. In previous
506   experimental studies (e.g., Morgan and Liang, 2005; Van den Bleeken et al., 2010; Tursack and
507   Liang, 2012; Wang et al., 2013; Saper and Liang, 2014), common mismatches in CaO
508   concentrations in olivine and pyroxenes were observed between field data and melt-rock reaction
509   experimental data: clinopyroxenes are higher in CaO while olivines and orthopyroxenes are more
510   depleted in CaO for the field data. These are attributed to subsolidus reequilibration of the field
511   samples and the high temperature nature of the dissolution experiments (>1200°C). Figures 6
512   and 7 show that CaO contents in olivine and pyroxenes from the hydrous reaction experiments
513   are close to those from the field observations, consistent with the low reaction and crystallization
514   temperatures in these experiments (1200°C to 880°C).

4.2. Amphiboles from mantle xenoliths

516   Figures 12a-12c compare compositions of amphibole obtained from the laboratory
517   experiments with those from mantle xenoliths. Amphiboles in the mantle xenoliths are mainly
518   pargasite and edenite with a small population being Mg-hornblende and tremolite. The main
519   composition range of amphibole in the mantle xenoliths overlaps that obtained from the melt-
520   rock reaction experiments (gray fields). Harzburgite xenoliths in andesites from Avacha,
521   Kamchatka (Bénard and Ionov, 2013) contain amphiboles in different lithological regions,
522   including the host harzburgite, orthopyroxene-rich veins that have reaction texture with host
523   harzburgite, and orthopyroxene-rich veins without reaction texture. The reaction texture between
524   the orthopyroxene-rich veins and the host harzburgite is similar to that observed around the
525   orthpyroxenite-peridotite interface in our experiments (Fig. 3). Amphiboles in the host
526   harzburgite and those in the veins with reaction texture (dark green squares) are mainly pargasite
527   and subordinately enenite and Mg-hornblende (Fig. 12a). Compositions of these amphiboles are
528   mainly in the range defined by the melt-rock reaction experiments (gray fields). The textural and
529   compositional features suggest that these veins were formed by reaction of peridotite and

530   hydrous melt in the lithospheric mantle (Bénard and Ionov, 2013). Amphiboles in the host
531   harzburgite were likely crystallized from reacting melt that infiltrated into the peridotite. In
532   contrast, the other type of orthopyroxene-rich veins crosscut the host harzburgite, and they have
533   a straight contact with the host harzburgite. Amphiboles in these veins (light green squares) are
534   mainly Mg-hornblende (Fig. 12a). They have low T-site Al, A-site Na, Ti abundances, and high
535   Mg#, varying along a trend defined by some amphiboles from phase equilibrium experiments
536   (thin green arrows in Fig. 12). The above evidence indicates that these veins are formed by direct
537   crystallization of the host andesitic melt during the transport of xenoliths to the surface.
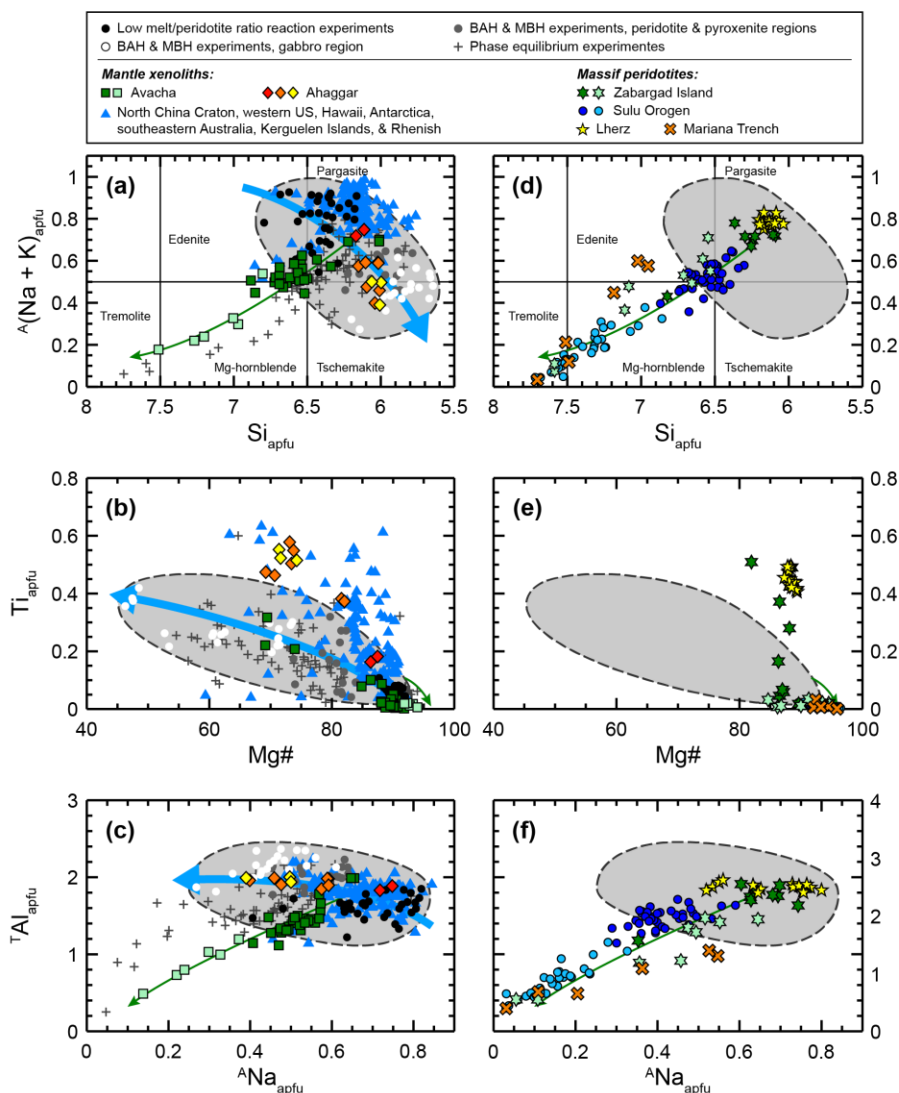

538

Figure 12. Plots of atomic compositions for amphiboles from the experiments and field observations of amphibole-
bearing mantle xenoliths (a-c) and massif peridotite (d-f). Calculation of chemical formula and division of
compositional boundaries (in a and d) follow Leake et al. (1997). The experimental data are shown as black dots
(low melt-to-rock ration reaction experiments, shown in Fig. 9), gray dots (peridotite and pyroxenite regions in
experiments from the present study), white dots (gabbronorite regions in experiments from the present study), and
gray plus symbols (phase equilibrium experiments, shown in Fig 9). The gray fields show composition range of
amphibole from melt-rock reaction experiments, and the thick blue arrows indicate the melt-rock reaction trend of
amphibole compositional variation. Source of the field data are the same as in Fig. 6. Amphiboles in peridotite
xenoliths and orthopyroxene-rich veins that have reaction texture with the host peridotite from Avacha are shown as
dark green squares, and those in orthopyroxene-rich veins without reaction texture are shown as light green squares.

549 Amphiboles in peridotite xenoliths, amphibole-rich veins and amphibolite xenoliths, and amphibole megacrysts
550 from Ahaggar are shown as red, orange, and yellow diamonds, respectively. Amphiboles from the other mantle
551 xenoliths are shown as blue triangles. Amphiboles in spinel peridotites and the amphibole-bearing bands associate
552 with secondary minerals in massif peridotites from Zabargad Island, are shown as dark green hexagons, and
553 amphiboles in the mylonitic share zones are shown as light green hexagons. Amphibole cores and rims from the
554 Sulu peridotites are shown as dark and light circles, respectively. Amphiboles in lherzolites and amphibolite veins
555 from the Lherz massif are shown as yellow pentagrams, and those in serpentinized peridotites from Mariana Trench
556 are shown as orange crosses. The thin green arrows indicate the compositional variation trend of amphiboles that
557 were likely formed by crystallization of host magma of mantle xenolith or by hydrothermal alteration at shallower
558 depths.

559   Different occurrences of amphiboles are also observed in a suit of mantle xenoliths and
560 megacrysts entrained by basalts from Ahaggar, southern Algeria (Dautria et al., 1987).
561 Amphiboles are present in peridotites with amphibole-rich veins, amphibolites, and as
562 megacrysts in the host basalt. Amphiboles are anhedral grains interstitial to anhydrous minerals
563 in the peridotites and oikocrysts that have chadacrysts of anhydrous minerals in the amphibole-
564 rich veins and amphibolites. Although amphibolite is not formed in the hydrous melt-rock
565 reaction experiments, the poikilitic texture of amphibole in the Ahaggar xenoliths is similar to
566 that observed in the peridotite region in the experiments (Fig. 2). Furthermore, amphiboles in the
567 Ahaggar xenoliths with different occurrences show a compositional variation along the trend
568 defined by the melt-rock reaction experiments (thick blue arrows in Fig. 12). Amphiboles in the
569 peridotites (red diamonds) are high in Mg# and low in Ti (Fig. 12b), similar to those in
570 ultramafic regions from our experiments (gray dots) and the low melt-to-rock ratio experiments
571 (black dots). Amphiboles in the amphibole-rich veins and amphibolites (orange diamonds) have
572 low Mg# and high Ti abundance (Fig. 12b), similar to the amphibole megacrysts in the host
573 basalt (yellow diamonds) and those in the gabbronorite region of our experiments (white dots).
574 The variations in occurrence and composition suggest that amphiboles in the Ahaggar peridotites
575 and amphibolites were formed by reactive crystallization when hydrous melts infiltrate
576 peridotite, and the amphibole megacrysts were crystallized from the reacted melt (Dautria et al.,
577 1987). The reaction trend is also observed in the amphibole-bearing lherzolites from Victoria
578 Land, Antarctica: amphibole disseminated in peridotite has a higher Mg# and a lower Ti
579 abundance than that in the amphibole veins, suggestive of melt-rock reaction origin of the
580 amphiboles with different melt-to-rock ratios (Coltorti et al., 2004).

581   4.3. Amphiboles from massif peridotites

582   Figures 12d-12f compare the experimental amphibole compositions with those from
583 massif peridotites. The massif peridotites from Zabargad Island, Red Sea contain amphiboles
584 interstitial to olivines in spinel peridotite, in bands associated with secondary spinel between
585 bands of olivines, and in mylonitic shear zones (Agrinier et al., 1993). Massif peridotites from
586 the Sulu Orogenic Belt, eastern China have amphiboles with core-to-rim compositional variation,
587 and inclusions of olivine, serpentine and spinel (Li et al., 2018). The peridotite sample from the
588 Lherz massif has an amphibolite vein. Modal abundance of amphibole increases from the host
589 peridotite towards the vein (Zanetti et al., 1996). Massif peridotite samples from the island arc at
590 Mariana Trench are serpentinized and contain tremolite, hornblende, and enenite (Fig. 12d)
591 (Ohara and Ishii, 1998). Compositionally, amphiboles in the spinel peridotite and the secondary
592 bands from Zabargad (dark green hexagons in Figs. 12d-12f), amphibole cores from Sulu (dark
593 blue circles), and amphiboles from Lherz (yellow pentagrams) are mainly in the composition
594 range of the melt-rock reaction experiments. This is consistent with the occurrences that these

595 amphiboles are interstitial or associated with secondary minerals, and supports the origin that
596 they are from by reaction of peridotite with hydrous melts (e.g., Agrinier et al., 1993; Zanetti et
597 al., 1996). Amphiboles in the mylonitic shear zones in the massif peridotites from Zabargad
598 (light green hexagons in Figs. 12d-12f), amphibole rims in the Sulu orogenic peridotite (light
599 blue circles in Figs. 12d-12f), and amphiboles in the serpentinized peridotites from Mariana
600 Trench (orange crosses, Ohara and Ishii, 1998) vary along the trend that is different from that
601 defined by the melt-rock reaction experiments (thin green arrows in Fig. 12d-12f). The
602 compositional variation and the occurrences of these amphiboles indicate that they were formed
603 by processes such as hydrothermal alteration (fluid-rock reaction) when the peridotites have
604 emplaced or exhumed at shallow depths (Agrinier et al., 1993; Ohara and Ishii, 1998; Li et al.,
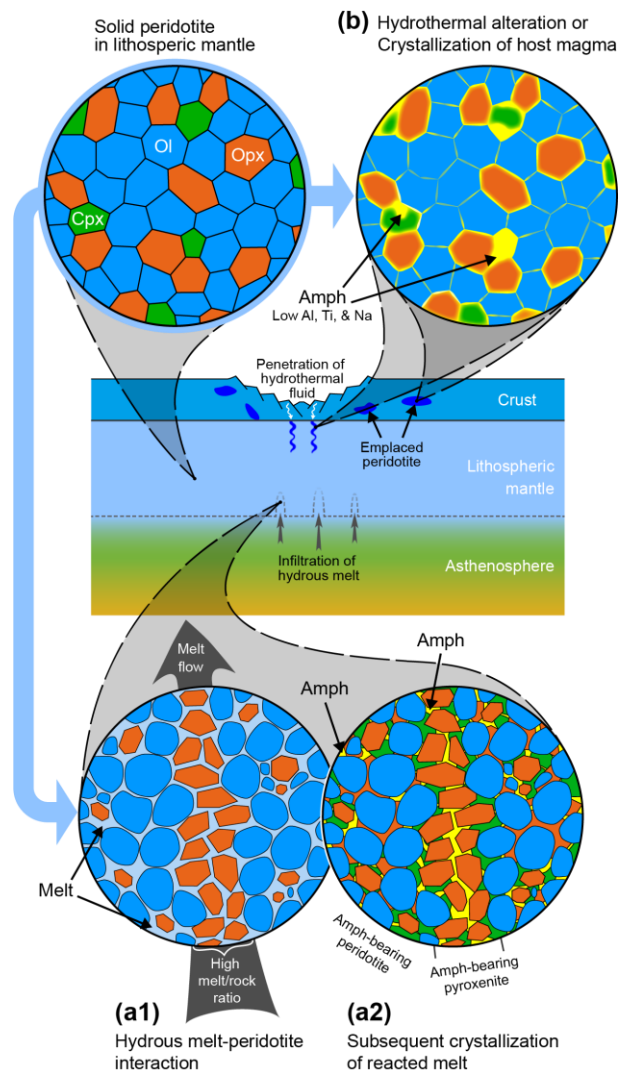605 2018).

606

607 **Figure 13.** Schematic diagrams illustrating scenarios where amphiboles are formed in the lithospheric mantle. (a1)
608 and (a2) show the processes leading to the formation of amphibole-bearing peridotite and pyroxenite by hydrous
609 melt-peridotite interaction. Hydrous melt infiltration initiates partial melting of the peridotite in lithospheric mantle.
610 Reaction between the hydrous melt and the peridotite forms orthopyroxene-depleted peridotite and orthopyroxene
611 vein or dike (a1). As the peridotite cooled, the interstitial melts crystallize clinopyroxene and amphibole with
612 composition varying along the trends established by the melt-rock reaction experiments forming amphibole-bearing
613 peridotite and pyroxenite (a2). (b) shows the formation of amphibole in peridotite by metamorphism. Hydrothermal

614 fluids penetrate peridotite at the crust-mantle boundary or in the lower crust after peridotite emplacement forming
615 amphibole with high Mg#, SiO_2, and CaO and low Al_2O_3, TiO_2, and Na_2O contents (magenta trends in Fig. 13). Ol =
616 olivine; Opx = orthopyroxene; Cpx = clinopyroxene; Amph = amphibole.

617 ### 4.4. Formation mechanisms of amphibole-bearing mantle rocks

618 The amphibole-bearing pyroxenite and amphibole-bearing peridotite that formed in the
619 hydrous melt-peridotite reaction experiments are similar to a number of field observations in
620 terms of texture, lithology, and mineral compositions, indicating that these field amphiboles are
621 likely formed by hydrous melt-peridotite interaction. The schematic diagram in Fig 13
622 summarizes mechanisms through which various amphiboles are formed in the lithospheric
623 mantle. Infiltration of hydrous melts may be focused either by means of hydro-fracturing or
624 reaction induced infiltration instability similar to the one that produces replacive dunite in the
625 mantle section of ophiolite (e.g., Kelemen et al., 1997). When a hydrous melt (or fluid) infiltrate
626 the lithospheric mantle along pressure gradients or fractures, it may induce partial melting of the
627 surrounding peridotite. Further reaction between the hydrous melt and the partially molten
628 peridotite produces a melt-bearing orthopyroxenite vein (Fig. 13a1, Wang et al., 2016). A new
629 generation of clinopyroxene and amphibole then precipitate from the trapped interstitial melts as
630 the peridotite is cooled or water in melt is released (by diffusion or change of pressure). The
631 precipitation may occur in the partially molten peridotite and the melt-bearing orthopyroxenite,
632 forming an amphibole-bearing peridotite and an amphibole-bearing pyroxenite, respectively
633 (Fig. 13a2). It can be inferred that the precipitation may form an amphibole-rich lithology in
634 reaction zone where the proportion of hydrous melt is high. The amphibolites from Ahaggar
635 (Dautria et al., 1987) and amphibole veins in lherzolites from Victoria Land (Coltorti et al.,
636 2004) may represent such examples.

637 However, not all amphiboles in mantle rocks are formed by melt-rock reaction.
638 Compositions of some amphiboles in natural samples are different from those produced by the
639 melt-rock reaction experiments (Fig. 12). These amphiboles grow as rims of amphiboles formed
640 by melt-rock reaction (e.g., Li et al., 2018), occur in veins that show not textural evidence of
641 reaction with the host peridotites (e.g., Agrinier et al., 1993; Bénard and Ionov, 2013), or present
642 in peridotite with evidence of hydrothermal alteration (e.g., Ohara and Ishii, 1998). They are
643 likely formed by processes such as crystallization of host magma of mantle xenoliths or
644 hydrothermal alteration after emplacement or exhumation of peridotite massifs at crustal depths
645 (Fig. 13b).

646 **5 Conclusions**

647 The role of hydrous melt-peridotite reaction in the formation of amphibole-bearing
648 mantle rocks is examined by reacting spinel lherzolite with a hydrous basaltic andesite and a
649 hydrous MORB (with 4 wt% water in the melts) in Au-Pd capsules using the reaction couple
650 method. The experiments include a reaction at 1200°C and 1 GPa and a further
651 reaction/crystallization through a series of step cooling to 880°C and 0.8 GPa. Results of the
652 hydrous melt-peridotite reaction experiments together with those conducted under anhydrous
653 conditions are used to deduce processes leading to the formation of amphibole in mantle rocks.
654 The main conclusions of this study are as follows:

1. Reaction between hydrous basaltic melt and lherzolite followed by in situ crystallization produces an amphibole gabbronorite, amphibole-bearing orthopyroxenite, and amphibole-bearing peridotite sequence.

2. A high-porosity orthopyroxenite-dunite sequence is formed in the reaction at 1200°C. Crystallization of orthopyroxene continues at the early stages of cooling, followed by clinopyroxene, and finally amphibole in the peridotite and orthopyroxenite.

3. Lithology, texture, and mineral compositional variation are key features that can be used to deduce the origin of amphiboles in peridotites and pyroxenites.

4. Similarities in these key features between the experiments reported in this study and those observed in amphibole-bearing mantle xenoliths and massif peridotites underscore the importance of hydrous melt-peridotite reaction and in situ crystallization in the formation of amphiboles in these mantle rocks.

5. Texture and compositional variations of some amphiboles from the field are distinct from those obtained from the melt-peridotite reaction experiments, including the low Ti, Al, and Na abundances. These amphiboles are likely formed by crystallization of xenoliths' host magma and hydrothermal alterations at shallow depths.

Acknowledgments

References

Agrinier, P., Mével, C., Bosch, D., & Javoy, M. (1993). Metasomatic hydrous fluids in amphibole peridotites from Zabargad island (Red Sea). *Earth and Planetary Science Letters*, 120, 187–205

Barr, J. A., & Grove, T. L. (2010). Au Pd Fe ternary solution model and applications to understanding the fO_2 of hydrous, high-pressure experiments. *Contributions to Mineralogy and Petrology*, 160, 631–643

Beck, A. R., Morgan, Z. T., Liang, Y., & Hess, P. C. (2006). Dunite channels as viable pathways for mare basalt transport in the deep lunar mantle. *Geophysical research letters*, 33, L01202

Bénard, A., & Ionov, D. A. (2013). Melt– and fluid–rock interaction in supra-subduction lithospheric mantle: Evidence from andesite-hosted veined peridotite xenoliths. *Journal of Petrology*, 54(11), 2339–2378

Bonadiman, C., Nazzareni, S., Coltorti, M., Comodi, P., Giuli, G., & Faccini, B. (2014). Crystal chemistry of amphiboles: Implications for oxygen fugacity and water activity in lithospheric mantle beneath Victoria land, Antarctica. *Contributions to Mineralogy and Petrology*, 167, 1–17

Borghini, G., Fumagalli, P., & Rampone, E. (2010). The stability of plagioclase in the upper mantle: subsolidus experiments on fertile and depleted lherzolite. *Journal of Petrology*, 51, 229–254

695 Brey, G. P., & Köhler, T. P. (1990) Geothermobarometry in four-phase lherzolites II. New
696 thermobarometers, and practical assessment of existing thermobarometers. *Journal of Petrology*
697 31, 1353-1378

698 Carroll, M. R., & Wyllie, P. J. (1989). Experimental phase relations in the system tonalite-
699 peridotite-H_2O at 15 kbar: Implications for assimilation and differentiation processes near crust-
700 mantle boundary. *Journal of Petrology*, 30,1351–1382

701 Clague, D. A., Bohrson, W. A. (1991). Origin of xenoliths in the trachyte at Puu Waawaa,
702 Hualapai volcano, Hawaii. *Contributions to Mineralogy and Petrology*, 108, 439–452

703 Coltorti, M., Beccaluva, L., Bonadiman, C., Faccini, B., Ntaflos, T., & Siena, F. (2004).
704 Amphibole genesis via metasomatic reaction with clinopyroxene in mantle xenoliths from
705 Victoria land, Antarctica. *Lithos*, 75, 115–139

706 Daines, M. J., Kohlstedt, D. L. (1994). The transition from porous to channelized flow due to
707 melt/rock reaction during melt migration. *Geophysical Research Letters*, 21, 145–148

708 Dautria, J. M., Liotard, J. M., Cabanes, N., Girod, M., & Briqueu, L. (1987). Amphibole-rich
709 xenoliths and host alkali basalts: Petrogenetic constraints and implications on the recent
710 evolution of the upper mantle beneath Ahaggar (Central Sahara, Southern Algeria).
711 *Contributions to Mineralogy and Petrology*, 95, 133–144

712 Ernst, W. G., & Liu, J. (1998). Experimental phase-equilibirium study of Al- and Ti-contents of
713 calcic amphibole in MORB-A semiquantitative thermobarometer. *American Mineralogist*, 83,
714 952–969.

715 Faak, K., Chakraborty, S., & Coogan, L. A. (2013). Mg in plagioclase: experimental calibration
716 of a new geothermometer and diffusion coefficients. *Geochimica et Cosmochimica Acta*, 123,
717 195–217

718 Feig, S. T., Koepke, J., & Snow, J. E. (2006). Effect of water on tholeiitic basalt phase equilibria:
719 An experimental study under oxidizing conditions. *Contributions to Mineralogy and Petrology*,
720 152, 611–638

721 Francis, D. M. (1976a). Amphibole pyroxenite xenoliths: cumulate or replacement phenomena
722 from the upper mantle, Nunivak island, Alaska. *Contributions to Mineralogy and Petrology*, 58,
723 51–61

724 Francis, D. M. (1976b). The origin of amphibole in lherzolite xenoliths from Nunivak island,
725 Alaska. *Journal of Petrology*, 17, 357–378

726 Frey, F. A., & Prinz, M. (1978). Ultramafic inclusions from San Carlos, Arizona: Petrologic and
727 geochemical data bearing on their petrogenesis. *Earth and Planetary Science Letters*, 38, 129–
728 176

729 Fumagalli, P., Borghini, G., Rampone, E., & Poli, E. (2017). Experimental calibration of
730 Forsterite–Anorthite–Ca-Tschermak–Enstatite (FACE) geobarometer for mantle peridotites.
731 *Contributions to Mineralogy and Petrology*, 172(6), 38

732 Green, T. H., & Pearson, N. J. (1985). Experimental determination of REE partition coefficients
733 between amphibole and basaltic to andesitic liquids at high pressure. *Geochimica et*
734 *Cosmochimica Acta*, 49, 1465–1468

735 Ishimaru, S., Arai, S., Ishida, Y., Shirasaka, M., & Okrugin, V. M. (2007). Melting and multi-
736 stage metasomatism in the mantle wedge beneath a frontal arc inferred from highly depleted
737 peridotite xenoliths from the Avacha volcano, Southern Kamchatka. *Journal of Petrology*, 48(2),
738 395–433

739 Johnston, A. D., & Wyllie, P. J. (1989). The system tonalite-peridotite-H_2O at 30 kbar, with
740 applications to hyperdization in subduction zone magmatism. *Contributions to Mineralogy and*
741 *Petrology*, 102, 257–264

742 Kelemen, P. B., Joyce, D. B., Webster, J. D., & Holloway, J. R. (1990). Reaction between
743 ultramafic rock and fractionating basaltic magma II. Experimental investigation of reaction
744 between olivine tholeiite and harzburgite at 1150–1050°C and 5 kb. *Journal of Petrology*, 31,
745 99–134

746 Kelemen, P. B., Hirth, G., Shimizu, N., Spiegelman, M., & Dick, H. J. B. (1997). A review of
747 melt migration processes in the adiabatically upwelling mantle beneath oceanic spreading ridges.
748 *Philosophical Transactions Mathematical Physical and Engineering Sciences*, 355, 283–318

749 Koepke, J., Schoenborn, S., Oelze, M., Wittmann, H., Feig, S. T., Hellebrand, E., Boudier, F., &
750 Schoenberg, R. (2009). Petrogenesis of crustal wehrlites in the Oman ophiolite: Experiments and
751 natural rocks. *Geochemisty Geophysics Geosystems*, 10, Q10002

752 Köhler, T. P., & Brey, G. P. (1990). Calcium exchange between olivine and clinopyroxene
753 calibrated as a geothermobarometer for natural peridotites from 2 to 60 kb with applications.
754 *Geochimica et Cosmochimica Acta*, 54, 2375–2388

755 Lambart, S., Laporte, D., & Schiano, P. (2009). An experimental study of focused magma
756 transport and basalt–peridotite interactions beneath mid-ocean ridges: Implications for the
757 generation of primitive MORB compositions. *Contributions to Mineralogy and Petrology*, 157,
758 429–451

759 Lambart, S., Laporte, D., Provost, A. & Schiano P. (2012). Fate of pyroxenite-derived melts in
760 the peridotitic mantle: thermodynamic and experimental constraints. *Journal of Petrology*, 53,
761 451–476

762 Larocque, J., & Canil, D. (2010). The role of amphibole in the evolution of arc magmas and
763 crust: the case from the Jurassic bonanza arc section, Vancouver Island, Canada. *Contributions*
764 *to Mineralogy and Petrology*, 159, 475–492

765 Latourrette, T., Hervig, R. L., & Holloway, J. R. (1995). Trace element partitioning between
766 amphibole, phlogopite, and basanite melt. *Earth and Planetary Science Letters*, 135, 13–30

767 Leake, B. E., Wooley, A. R., Arps, C. E., Birch, W. D., Gilbert, M. C., Grice, J. D., Hawthorne,
768 E. C., Kato, A., Kisch, HJ., Krivovichev, V. G., Linthout, K., Laird, J., Maresch, W. V., Nickel,
769 E. H., Schumacher, J. C., Smith, D. C., Stephenson, N. C. N., Whittaker, E. J. W., & Guo., Y.,
770 (1997). Nomenclature of amphiboles; report of the Subcommittee on amphiboles of the
771 International Mineralogical Association Commission on New Minerals and Mineral Names.
772 *European Journal of Mineralogy*, 9, 623–651

773 Li, H., Chen, R., Zheng, Y., Hu, Z., & Xu, L. (2018). Crustal metasomatism at the slab-mantle
774 interface in a continental subduction channel: Geochemical evidence from orogenic peridotite in
775 the Sulu Orogen. *Journal of Geophysical Research: Solid Earth*, 123, 2174–2198

776 Longhi, J., Walker, D., & Hays, F. (1976). Fe and Mg in plagioclase. Proceedings of the 7th
777 Lunar Science Conference, Houston, TX, 15–19, March. pp, 1281–1300

778 Mallik, A., Nelson, J., & Dasgupta, R. (2015). Partial melting of fertile peridotite fluxed by
779 hydrous rhyolitic melt at 2–3 GPa: Implications for mantle wedge hybridization by sediment
780 melt and generation of ultrapotassic magmas in convergent margins. *Contributions to
781 Mineralogy and Petrology*, 169, 1–24

782 Mandler, B. E., & Grove, T. L. (2016). Controls on the stability and composition of amphibole in
783 the Earth's mantle. *Contributions to Mineralogy and Petrology*, 171, 68

784 Mercer, C. N., & Johnston, A. D. (2008). Experimental studies of the P–T–H_2O near-liquidus
785 phase relations of basaltic andesite from North Sister Volcano, High Oregon Cascades:
786 Constraints on lower-crustal mineral assemblages. *Mineralogy and Petrology*, 155, 571–592

787 Moine, B. N., Grégoire, M., O'Reilly, S. Y., Sheppard, S. M. F., & Cottin, J. Y. (2001). High
788 field strength element fractionation in the upper mantle: Evidence from amphibole-rich
789 composite mantle xenoliths from the Kerguelen Islands (Indian Ocean). *Journal of Petrology*,
790 42, 2145–2167

791 Morgan, Z., & Liang, Y. (2003). An experimental and numerical study of the kinetics of
792 harzburgite reactive dissolution with applications to dunite dike formation. *Earth and Planetary
793 Science Letters,* 214, 59–74

794 Morgan, Z., & Liang, Y. (2005). An experimental study of the kinetics of lherzolite reactive
795 dissolution with applications to melt channel formation. *Contributions to Mineralogy and
796 Petrology*, 150, 369–385

797 Namur, O., Charlier, B., Toplis, M. J., & Auwera, J. V. (2012). Prediction of plagioclase-melt
798 equilibria in anhydrous silicate melts at 1-Atm. *Contributions to Mineralogy and Petrology*, 163,
799 133–150

800 Nandedkar, R. H., Hürlimann, N., Ulmer. P., & Müntener, O. (2016). Amphibole–melt trace
801 element partitioning of fractionating calc-alkaline magmas in the lower crust: An experimental
802 study. *Contributions to Mineralogy and Petrology*, 171, 71

803 Nicholls, I. A., & Harris, K. L. (1980). Experimental rare earth element partition coefficients for
804 garnet, clinopyroxene and amphibole coexisting with andesitic and basaltic liquids. *Geochimica
805 et Cosmochimica Acta*, 44, 287–308

806 Niida, K., & Green, D. H. (1999). Stability and chemical composition of pargasitic amphibole in
807 morb pyrolite under upper mantle conditions. *Contributions to Mineralogy and Petrology*, 135,
808 18–40.

809 Ohara, Y., & Ishii, T. (1998). Peridotites from the southern Mariana forearc: Heterogeneous fluid
810 supply in mantle wedge. *Island Arc*, 7, 541–558

811 O'Reilly, S. Y., Griffin, W. L., & Ryan, C. G. (1991). Residence of trace elements in
812 metasomatized spinel lherzolite xenoliths: A proton-microprobe study. *Contributions to
813 Mineralogy and Petrology*, 109, 98–113

814 Parat, F., Holtz, F., & Feig, S. (2008). Pre-eruptive conditions of the Huerto andesite (Fish
815 Canyon system, San Juan volcanic field, Colorado): Influence of volatiles (C–O–H–S) on phase
816 equilibria and mineral composition. *Journal of Petrology*, 49, 911–935

817 Pietranik, A., Holtz, F., Koepke, J., & Puziewicz, J. (2009). Crystallization of quartz dioritic
818 magmas at 2 and 1 kbar: Experimental results. *Mineralogy and Petrology*, 97, 1–21

819 Powell, W., Zhang, M., O'Reilly, S. Y., & Tiepolo, M. (2004). Mantle amphibole trace-element
820 and isotopic signatures trace multiple metasomatic episodes in lithospheric mantle, Western
821 Victoria, Australia. *Lithos*, 75(1), 141–171

822 Rapp, R. P., Shimizu, N., Norman, M. D., & Applegate, G. S. (1999). Reaction between slab-
823 derived melts and peridotite in the mantle wedge: experimental constraints at 3.8 GPa. *Chemical*
824 *Geology*, 160, 335–356

825 Saper, L., & Liang, Y. (2014). Formation of plagioclase-bearing peridotite and plagioclase-
826 bearing wehrlite and gabbro suite through reactive crystallization: An experimental study.
827 *Contributions to Mineralogy and Petrology*, 167, 985

828 Sekine, T., & Wyllie, P. J. (1983). Experimental simulation of mantle hybridization in
829 subduction zones. *The Journal of Geology*, 91, 511–528

830 Sen, C., & Dunn, T. (1994). Experimental modal metasomatism of a spinel lherzolite and the
831 production of amphibole-bearing peridotite. *Contributions to Mineralogy and Petrology*, 119,
832 422–432

833 Spear, F. J. (1981). An experimental study of hornblende stability and compositional variability
834 in amphibole. American Journal of Science 281, 697–734.

835 Takahashi, E., & Nakajima, K. (2002). Melting process in the Hawaiian plume: an experimental
836 study. *American Geophysical Union Monograph*, 128, 403–418

837 Takagi, D., Sato, H., & Nakagawa, M. (2005). Experimental study of a low-alkali tholeiite at 1–5
838 kbar: optimal condition for the crystallization of high-An plagioclase in hydrous arc tholeiite.
839 *Contributions to Mineralogy and Petrology*, 149, 527–540

840 Tursack, E., & Liang, Y. (2012). A comparative study of melt-rock reactions in the mantle:
841 Laboratory dissolution experiments and geological field observations. *Contributions to*
842 *Mineralogy and Petrology*, 163, 861–876

843 Van den Bleeken, G., Muntener, O., & Ulmer, P. (2010). Reaction processes between tholeiitic
844 melt and residual peridotite in the uppermost mantle: An experimental study at 0.8 GPa. *Journal*
845 *of Petrology*, 51, 153–183

846 Van den Bleeken, G., & Muntener, O., Ulmer, P. (2011). Melt variability in percolated
847 peridotite: An experimental study applied to reactive migration of tholeiitic basalt in the upper
848 mantle. *Contributions to Mineralogy and Petrology*, 161, 921–945

849 Wang, C., Liang, Y., Xu, W., & Dygert, N. (2013). Effect of melt composition on basalt and
850 peridotite interaction: laboratory dissolution experiments with applications to mineral
851 compositional variations in mantle xenoliths from the North China Craton. *Contributions to*
852 *Mineralogy and Petrology*, 166, 1469–1488

853 Wang, C., Liang, Y., Dygert, N., & Xu, W. (2016). Formation of orthopyroxenite by reaction
854 between peridotite and hydrous basaltic melt: An experimental study. *Contributions to*
855 *Mineralogy and Petrology*, 171, 77

856 Weaver, S. L., Wallace, P. J., & Johnston, A. D. (2011). A comparative study of continental vs.
857 intraoceanic arc mantle melting: experimentally determined phase relations of hydrous primitive
858 melts. *Earth and Planetary Science Letters*, 308, 97–106

859 Wilshire, H. G., Calk, L. C., & Schwarzman, E. C. (1971). Kaersutite — a product of reaction
860 between pargasite and basanite at Dish Hill, California. *Earth and Planetary Science Letters*, 10,
861 281–284

862 Wilshire, H. G., Pike, J. E. N., Meyer, C. E., & Schwarzman, E. C. (1980). Amphibole-rich veins
863 in lherzolite xenoliths, Dish Hill and Deadman Lake, California. *American Journal of Science*,
864 280(A), 576–593

865 Witt, G., & Seck, H. A. (1989). Origin of amphibole in recrystallized and porphyroclastic mantle
866 xenoliths from the Rhenish Massif: Implications for the nature of mantle metasomatism. *Earth
867 and Planetary Science Letters*. 91(3), 327–340

868 Witt-Eickschen, G., Seck, H. A., Mezger, K., Eggins, S.M., & Altherr, R. (2003). Lithospheric
869 mantle evolution beneath the Eifel (Germany): Constraints from Sr–Nd–Pb isotopes and trace
870 element abundances in spinel peridotite and pyroxenite xenoliths. *Journal of Petrology*, 44(6),
871 1077–1095

872 Xu, W., Yang, D., Gao, S., Pei, F., & Yu, Y. (2010). Geochemistry of peridotite xenoliths in
873 early cretaceous High-Mg# diorites from the central orogenic block of the North China Craton:
874 The nature of Mesozoic lithospheric mantle and constraints on lithospheric thinning. *Chemical
875 Geology*, 270, 257–273

876 Xu, Y., & Bodinier, J. (2004). Contrasting enrichments in high- and low-temperature mantle
877 xenoliths from Nushan, Eastern China: Results of a single metasomatic event during lithospheric
878 accretion? *Journal of Petrology*, 45, 321–341

879 Yaxley, G. M., & Green, D. H. (1998). Reactions between eclogite and peridotite: mantle
880 refertilisation by subduction of oceanic crust. *Schweizerische Mineralogische Und
881 Petrographische Mitteilungen*, 78, 243–255

882 Zanetti, A., Vannucci, R., Bottazzi, P., Oberti, R., & Ottolini, L. (1996). Infiltration
883 metasomatism at Lherz as monitored by systematic ion-microprobe investigations close to a
884 hornblendite vein. *Chemical Geology*, 134, 113–133